



Structure of the RZZ complex and molecular basis of Spindly-driven corona assembly at human kinetochores

Tobias Raisch^{1,†} , Giuseppe Ciossani^{2,†,‡}, Ennio d'Amico^{2,†} , Verena Cmentowski^{2,†} , Sara Carmignani², Stefano Maffini², Felipe Merino^{1,§}, Sabine Wohlgemuth², Ingrid R Vetter^{2,*} , Stefan Raunser^{1,**}  & Andrea Musacchio^{2,3,***} 

Abstract

In metazoans, a ≈ 1 megadalton (MDa) multiprotein complex comprising the dynein–dynactin adaptor Spindly and the ROD–Zwilch–ZW10 (RZZ) complex is the building block of a fibrous biopolymer, the kinetochore fibrous corona. The corona assembles on mitotic kinetochores to promote microtubule capture and spindle assembly checkpoint (SAC) signaling. We report here a high-resolution cryo-EM structure that captures the essential features of the RZZ complex, including a farnesyl-binding site required for Spindly binding. Using a highly predictive *in vitro* assay, we demonstrate that the SAC kinase MPS1 is necessary and sufficient for corona assembly at supercritical concentrations of the RZZ–Spindly (RZZS) complex, and describe the molecular mechanism of phosphorylation-dependent filament nucleation. We identify several structural requirements for RZZS polymerization in rings and sheets. Finally, we identify determinants of kinetochore localization and corona assembly of Spindly. Our results describe a framework for the long-sought-for molecular basis of corona assembly on metazoan kinetochores.

Keywords centromere; fibrous corona; kinetochore; RZZ; spindle assembly checkpoint

Subject Categories Cell Cycle

DOI 10.15252/embj.2021110411 | Received 10 December 2021 | Revised 9 March 2022 | Accepted 11 March 2022 | Published online 4 April 2022

The EMBO Journal (2022) 41: e110411

Introduction

Kinetochores are multisubunit macromolecular assemblies that promote the bi-orientation and segregation of chromosomes during cell division (Musacchio & Desai, 2017; Navarro & Cheeseman, 2021). They are multilayered structures built on specialized chromatin loci named centromeres. The kinetochore's inner layer, named the constitutive centromere-associated network (CCAN), binds directly to the centromeric chromatin. The kinetochore's outer layer, named the Knl1 complex, Mis12 complex, Ndc80 complex (KMN) network, generates a microtubule-binding interface. Additionally, the KMN network is a functional platform for the recruitment of several proteins that regulate the process of chromosome bi-orientation. Among the latter are proteins participating in the spindle assembly checkpoint (SAC), a cell cycle checkpoint that prevents mitotic exit before completion of bi-orientation (Lara-Gonzalez *et al*, 2021). The SAC is essential for genome stability as it prevents the catastrophic effects of premature loss of chromosome cohesion in the presence of unattached chromosomes (Lara-Gonzalez *et al*, 2021).

In metazoans, including humans, checkpoint activity is coupled with the assembly of an outermost kinetochore layer named the kinetochore corona (Jokelainen, 1967; Rieder & Alexander, 1990; McEwen *et al*, 1993; Cooke *et al*, 1997; Yao *et al*, 1997; Hoffman *et al*, 2001; Magidson *et al*, 2015). The corona is a fibrous crescent-shaped structure that is only formed transiently in prometaphase cells, before the achievement of end-on attachment of chromosomes to microtubules (Kops & Gassmann, 2020). In checkpoint arrested cells, for instance in cells treated with agents, such as nocodazole, that promote microtubule depolymerization, the corona assumes a very characteristic expanded crescent shape that surrounds the core

¹ Department of Structural Biochemistry, Max Planck Institute of Molecular Physiology, Dortmund, Germany

² Department of Mechanistic Cell Biology, Max Planck Institute of Molecular Physiology, Dortmund, Germany

³ Centre for Medical Biotechnology, Faculty of Biology, University Duisburg-Essen, Essen, Germany

*Corresponding author. Tel: +49 231 133 2737; E-mail: ingrid.vetter@mpi-dortmund.mpg.de

**Corresponding author. Tel: +49 231 1332300; E-mail: stefan.raunser@mpi-dortmund.mpg.de

***Corresponding author. Tel: +49 231 1332101; E-mail: andrea.musacchio@mpi-dortmund.mpg.de

[†]These authors contributed equally to this work

[‡]Present address: European Institute of Oncology, Milan, Italy

[§]Present address: Department of Protein Evolution, Max Planck Institute for Developmental Biology, Tübingen, Germany

kinetochore and often even fuses with the corona nucleated by the sister kinetochore (Hoffman *et al*, 2001; Magidson *et al*, 2015; Wynne & Funabiki, 2015; Pereira *et al*, 2018; Sacristan *et al*, 2018).

In recent years, there has been substantial progress on the investigation of the mechanisms of assembly and disassembly of the kinetochore corona, and of its contributions to microtubule binding and SAC regulation (Kops & Gassmann, 2020). Proteins whose recruitment to kinetochore has been associated with assembly of the corona include the 3-subunit ROD–Zwilch–ZW10 complex (named after the *Drosophila melanogaster* genes *Rough Deal*, *Zwilch*, and *Zeste White 10*, and abbreviated as RZZ), the microtubule plus-end directed motor CENP-E, the microtubule-binding protein CENP-F, a tight “core complex” of the SAC proteins MAD1 and MAD2, and the microtubule minus-end-directed motor dynein, in complex with its processivity factor dynactin (dynein–dynactin will be abbreviated as DD) and with a DD adaptor named Spindly (Karess, 2005; Kops & Gassmann, 2020).

Microtubule motors in the corona facilitate the process of chromosome alignment at the metaphase plate. After initial microtubule capture, these motors coordinate minus- and plus-end-directed transport of chromosomes that promotes their alignment at the metaphase plate before conversion of kinetochore attachment from lateral (i.e., to the microtubule lattice) to end-on (i.e., into the kinetochore interface). This conversion engages the core microtubule receptor of the kinetochore, the NDC80 complex, a subcomplex of the KMN network. A crucial aspect of the lateral to end-on conversion is that it coincides with a sudden activation of DD and with the disassembly of the kinetochore corona, in a process traditionally known as “shedding” or “stripping” (Williams *et al*, 1996; Howell *et al*, 2001; Wojcik *et al*, 2001; Basto *et al*, 2004; Mische *et al*, 2008; Varma *et al*, 2008; Sivaram *et al*, 2009; Auckland *et al*, 2020).

Corona shedding also coincides with silencing of SAC signaling at the particular kinetochore undergoing conversion to end-on attachment (Kuhn & Dumont, 2017, 2019). The corona promotes the SAC by providing a docking site for the recruitment of the MAD1: MAD2 core complex, which is crucially required for checkpoint signaling (De Antoni *et al*, 2005; Faesen *et al*, 2017). SAC silencing is therefore caused by the removal, during corona shedding, of the MAD1: MAD2 core complex, which ultimately suppresses catalytic assembly of the checkpoint effector, the mitotic checkpoint complex (MCC) (Basto *et al*, 2000; Buffin *et al*, 2005; Kops *et al*, 2005; Fava *et al*, 2011; Matson & Stukenberg, 2014; Caldas *et al*, 2015; Silio *et al*, 2015; Zhang *et al*, 2015; Rodriguez-Rodriguez *et al*, 2018; Allan *et al*, 2020; Jackman *et al*, 2020).

The 812-kDa RZZ complex, whose subunits are shown schematically in Fig 1A, is a 2:2:2 hexamer (Scaerou *et al*, 2001; Civril *et al*, 2010; Mosalaganti *et al*, 2017). The RZZ is considered the corona’s building block (Mosalaganti *et al*, 2017; Pereira *et al*, 2018; Sacristan *et al*, 2018). While there is considerable interest in understanding how the RZZ promotes corona assembly, there is only limited structural insight into this process. An early structural analysis revealed the crystal structure of Zwilch and identified the 2,209-residue ROD protein as a member of a family of proteins, which also includes clathrin, consisting of an N-terminal β -propeller followed by a long α -solenoid (Civril *et al*, 2010). Reconstitution of the RZZ and a single-particle electron cryo-microscopy (cryo-EM) structure, limited to an average resolution of approximately 10–12 Å, offered the first comprehensive view of the organization of the RZZ hexamer (Altenfeld *et al*, 2015; Mosalaganti *et al*, 2017). The reconstruction demonstrated that two highly elongated ROD protomers are arranged in an anti-parallel configuration and that a ZW10 dimer cements this organization in its central region, while Zwilch occupies a more peripheral position, between ZW10 and the ROD β -propeller (Mosalaganti *et al*, 2017). Also based on homologous proteins of known structure but very limited sequence homology, structural models were built for ROD and ZW10 to fit the EM reconstruction (Mosalaganti *et al*, 2017). This previous work, however, failed to provide a detailed molecular description of the RZZ subunits and of their interactions. Here, we fill this gap by reporting a high-resolution structure of the RZZ complex, obtained by single-particle cryo-EM that finally reveals all its detailed structural features.

Spindly is a member of a large family of DD adaptors (Reck-Peterson *et al*, 2018) shown to activate dynein motility *in vitro* (McKenney *et al*, 2014; Schlager *et al*, 2014; Cianfrocco *et al*, 2015; Hoogenraad & Akhmanova, 2016; Gama *et al*, 2017; Pereira *et al*, 2018; Sacristan *et al*, 2018). How Spindly coordinates its interaction with RZZ with activation of DD motility and processivity remains poorly understood. Spindly binds directly to the RZZ complex through its C-terminal region (forming the complex abbreviated as RZZS), and engaging an RZZ module comprising the ROD β -propeller and Zwilch (Gama *et al*, 2017; Mosalaganti *et al*, 2017; Pereira *et al*, 2018; Sacristan *et al*, 2018; Henen *et al*, 2021). Furthermore, in humans and likely most other metazoans, Spindly is post-translationally modified on Cys602 with farnesyl, an isoprenoid lipid. This modification, which is required for the interaction of Spindly with RZZ, may engage a dedicated binding site on the ROD β -propeller (Holland *et al*, 2015; Moudgil *et al*, 2015; Gama *et al*, 2017; Mosalaganti *et al*, 2017).

Figure 1. Structural organization of the RZZ complex.

- Schematic representation of human RZZ subunits.
- 3D reconstruction of the RZZ complex with densities corresponding to ROD-A, Zwilch-A, and ZW10-A colored in firebrick, yellow-orange, and deep blue, respectively. ROD-B, Zwilch-B, and ZW10-B are displayed in equivalent lighter colors as indicated.
- Cartoon model of the RZZ complex with coloring scheme like in panel A. The position of the internal twofold axis of the 2:2:2 hexamer is shown. The N- and C-termini of ROD are indicated. Panels B-E and all other panels displaying molecular features were generated with PyMOL (The PyMOL Molecular Graphics System, version 1.2r3pre; Schrödinger, LLC).
- 90-degree-rotated view of the complex with linear dimensions.
- The conservation of residues in an alignment of ROD, Zwilch, and ZW10 is displayed on the surface of the complex (dark, highly conserved; light, poorly conserved). For all subunits, conservation was calculated from an alignment of sequences from *C. elegans* (Ce), *D. melanogaster* (Dm), *X. tropicalis* (Xt), *D. rerio* (Dr), *Bos taurus* (Bt), *Mus musculus* (Mm), and *Homo sapiens* (Hs).
- 180-degree-rotated view of the complex. The highest degree of conservation is observed in ZW10. See also alignments in Appendix Fig S2.

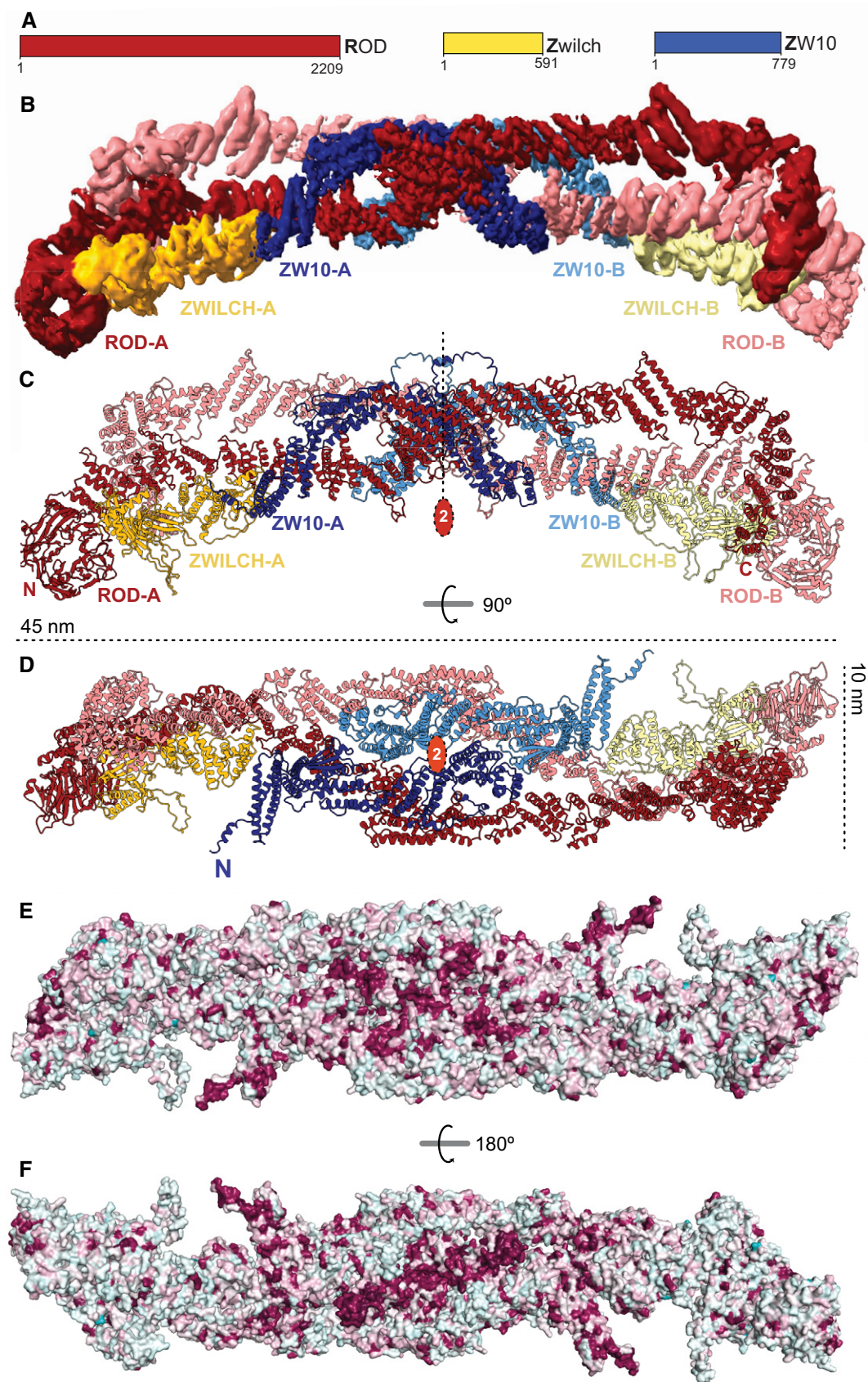


Figure 1.

Besides interacting with RZZ, Spindly is also required for kinetochore recruitment of DD (Starr *et al*, 1998; Griffis *et al*, 2007; Gassmann *et al*, 2008, 2010; Yamamoto *et al*, 2008; Chan *et al*, 2009; Barisic *et al*, 2010; Cheerambathur *et al*, 2013; Raaijmakers *et al*, 2013; Gama *et al*, 2017). The determinants of RZZ binding and DD recruitment by Spindly are separable. A region of Spindly, the Spindly motif, shown to be a conserved feature of adaptors, can be mutated to abrogate kinetochore recruitment of DD (Gassmann *et al*, 2010; Gama *et al*, 2017; Pereira *et al*, 2018; Sacristan *et al*, 2018). The mutation is compatible with corona expansion and chromosome bi-orientation, but preventing DD recruitment leads to a permanent SAC arrest caused by the inability to disassemble (strip) the corona and silence the SAC (Gassmann *et al*, 2010; Gama *et al*, 2017; Pereira *et al*, 2018; Sacristan *et al*, 2018).

Initial studies in humans and *C. elegans* identified conditions *in vitro* and in living cells for RZZ assembly into filamentous structural mimics of the corona, pointing to the RZZ as a candidate building block of the corona (Pereira *et al*, 2018; Sacristan *et al*, 2018; Henen *et al*, 2021). These recent studies, however, also brought to light different minimal requirements for filament assembly (Pereira *et al*, 2018; Sacristan *et al*, 2018), with species-specific differences and a persisting question on whether Spindly is necessary for filament assembly and acts as gatekeeper in this process. Corona assembly is limited to kinetochores and is sensitive to the cellular concentration of RZZ (Pereira *et al*, 2018), suggesting it requires a critical concentration that is exclusively reached upon RZZ recruitment to kinetochores in early prometaphase. Kinetochore recruitment, however, is not sufficient for corona assembly in human cells, because the depletion of Spindly or the inhibition of the SAC kinase MPS1 prevents expansion of the corona without preventing kinetochore recruitment of the RZZ (Pereira *et al*, 2018; Rodriguez-Rodriguez *et al*, 2018). Here, we have recapitulated with purified components *in vitro* the requirement for human ROD phosphorylation by MPS1 and Spindly binding for corona assembly. This assay allowed us to identify various additional requirements for nucleation of filaments by the RZZS complex, and to acquire structural information on the mechanism of filament assembly that was related to the high-resolution structure of the RZZ. We present a model for corona assembly whose implications were extensively corroborated with experiments in mitotic cells. Collectively, our results greatly advance our understanding of a fundamental aspect of kinetochore structure and function.

Results

Reconstitution and structural analysis of the RZZ complex

Using reconstituted human RZZ (Altenfeld *et al*, 2015; Mosalaganti *et al*, 2017), we previously reported a single-particle cryo-EM reconstruction of the RZZ at an overall resolution of $\sim 10\text{--}12$ Å (1 Å = 0.1 nm). As only the structure of Zwilch (Civril *et al*, 2010) (PDB ID 3IF8) had been experimentally determined, we had tried to account for the observed density by building *ad hoc* homology models of ROD or ZW10 and fitting them in the 3D reconstruction (Mosalaganti *et al*, 2017). Due to the very low resolution of the reconstructions, however, the resulting models were merely tenta-

To improve the resolution of the RZZ structure, we used a mCherry-tagged RZZ construct ($^{\text{mCh}}$ RZZ) that was better expressed than the previously used poly-histidine-tagged RZZ (see Methods). In addition, purified $^{\text{mCh}}$ RZZ proved to be more stable than the previous construct, allowing us to determine the structure of the complex by cryo-EM at a resolution of 3.9 Å (Fig 1B). The new reconstruction allowed us to build an essentially complete atomic model of ZW10 and the central region of ROD. In the periphery of RZZ, where the resolution of the reconstruction was lower than in the center and therefore did not allow unequivocal model building, we resorted to high-confidence AlphaFold2 (AF2; Jumper *et al*, 2021; Tunyasuvunakool *et al*, 2021) predictions, and used flexible fitting with minimal interventions, to fit them in the density (Fig EV1A–D).

While related to our previous low-resolution model in its general outline, the new model provides a detailed description of all crucial molecular features of the RZZ complex. The RZZ complex is a 2:2:2 hexamer with C2 symmetry. The twofold-related ROD chains (A and B) run in an anti-parallel configuration that sets the $\sim 45\text{-nm}$ -long and $\sim 10\text{-nm}$ -wide dimensions of the RZZ (Fig 1C and D). After an N-terminal 7-bladed β -propeller, the ROD chain transitions, near residue 395, into a short helical hairpin that begins an uninterrupted but irregular α -solenoid that extends until the C-terminus.

Several proteins share with ROD a succession of an N-terminal β -propeller followed by a C-terminal α -solenoid. These include clathrin, COP1, the Nup155 and Nup145 nucleoporins, Sec31, Sec39, and even the APC1 subunit of the APC/C (ter Haar *et al*, 1998; Fotin *et al*, 2004; Stagg *et al*, 2006, 2007; Fath *et al*, 2007; Brohawn *et al*, 2008; Lee & Goldberg, 2010; Alfieri *et al*, 2017; Watson *et al*, 2019). In comparison with the 1,675-residue clathrin heavy chain or the 1,944-residue APC1, the 2,209-residue ROD α -solenoid is significantly more elongated and straighter (Appendix Fig S1). The packing of successive helical hairpins against each other with a slight right- or a left-handed rotation is a typical pattern of regular α -solenoids. This pattern is also observed for blocks of successive helical hairpins in ROD, but there are points where the hairpins rather pack almost at a right angle, deflecting the polypeptide chain (Appendix Fig S1). There are at least three points where the ROD chain bends sharply, around residues 856 and 1,060 in the central region, and around residue 1905 in the C-terminal region. The latter kink generates a characteristic C-terminal “hook” that is perpendicular to the opposite ROD chain (Fig 2A and Appendix Fig S1A). This is a prominent interaction interface between ROD-A and ROD-B, as residues 1,790–2,125, which encompass part of the hook domain, form a cradle that interacts with residues 505–690 of the opposing ROD protomer, including residues 655–680, situated in an interhelical loop (Fig 2B).

Zwilch abuts the ROD β -propeller and forms a direct, extensive interface with only one of the ROD protomers, with only a small contact with the hook domain of the second ROD molecule (Fig 2C). Contacts of Zwilch with ROD terminate around residue 850 of ROD, where Zwilch also contacts ZW10 in a small 3-way interface. As expected, the structure of Zwilch in the RZZ complex is closely related to the crystal structure of Zwilch obtained in isolation (Civril *et al*, 2010), but adopts a more open conformation due to a reciprocal rotation of Zwilch’s two domains, presumably elicited by contacts within the complex (Appendix Fig S1B).

Finally, ZW10 adopts a highly curved, U-shaped conformation, a major determinant of which is the sharp bending around residue

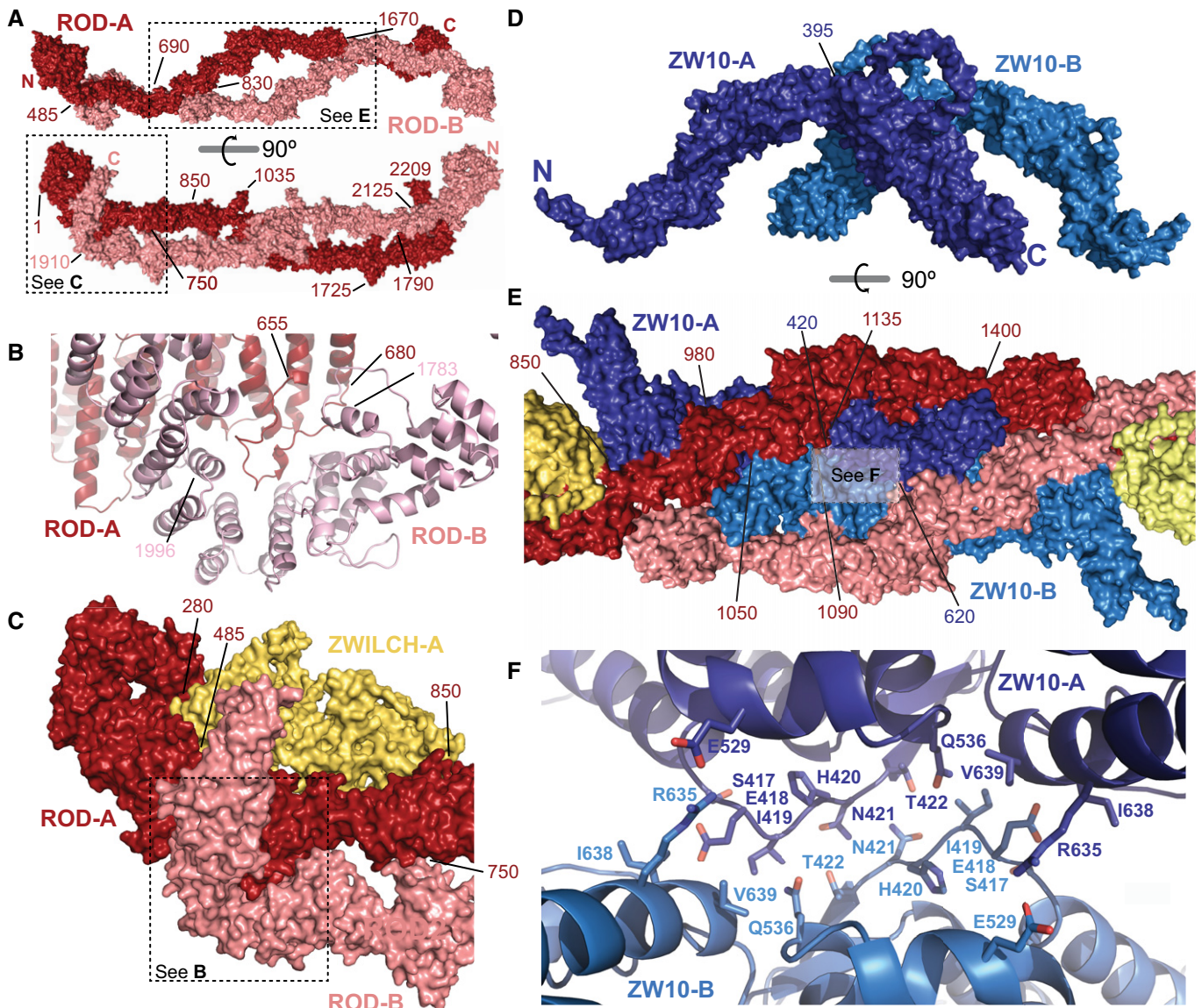


Figure 2. Homo- and heterotypic intermolecular interactions in RZZ.

- A The ROD-A and ROD-B protomers are related by twofold symmetry and interact through two main regions positioned between residues 485–690 and 1,790–2,125.
- B A particular prominent interaction between ROD-A and ROD-B consists in the insertion of the 655–680 loop of one protomer into a cradle formed by the bending C-terminal region of the second protomer.
- C Zwilch interacts very prominently with only one of the two ROD protomers, sandwiched between the N-terminal β -propeller and residue 850. A few interactions also link Zwilch to the C-terminal region of the second protomer.
- D A rotated view shows that ZW10 forms a highly bent, U-shaped complex with a relatively small interprotomer interface.
- E The twofold axis of the complex (shown in Fig 1B) crosses the interface between ZW10-A and ZW10-B.
- F Molecular details of the interface between ZW10-A and ZW10-B with side chains of residues involved.

395, situated between the N- and C-terminal domains (Fig 2D and Appendix Fig S1C). ZW10-related domains are found in Dsl1 and Tip20, subunits of vesicle tethering complexes in *S. cerevisiae*. Like ZW10, they both consist of two roughly equally sized helical domains (Tripathi *et al*, 2009), but are characterized by different interdomain angles (Appendix Fig S1D). Indeed, the isolated ZW10 shows high flexibility between its two domains (Mosalaganti *et al*, 2017).

In the RZZ, the interface between the A and B protomers of ZW10, which intersects the twofold symmetry axis of the RZZ complex, is relatively small (Fig 2D–F). Accordingly, while AF2 predicts the structure of ZW10 with remarkable accuracy (Appendix Fig S1E), it does not predict any solitary ZW10 dimer in a conformation seen in the RZZ complex (unpublished results). ZW10-A and ZW10-B, however, are stably set inside an “eye” between the two ROD chains (compare panels A and E in Fig 2), with which

they form a very extensive interaction interface. Specifically, residues 850–980, 1,050–1,090, and 1,135–1,400 of ROD-A interact with ZW10-A, ZW10-B, and ZW10-A, respectively. The N-terminal regions of ZW10 are prominent features that emerge almost perpendicularly from the RZZ's long axis. Together with the C-terminal region of ZW10, they are among the best conserved sequence features of the RZZ complex (Fig 1E and F; alignments are provided in Appendix Fig S2).

ROD's farnesyl-binding site

The interaction of Spindly with RZZ is direct and requires isoprenylation of Spindly with a farnesyl group at Cys602 (Mosalaganti *et al*, 2017) (Fig 3A). With farnesyl moieties modified with photoactivatable cross-linkers and enzymatically incorporated in Spindly, we previously mapped a farnesyl-binding site near Leu120 of ROD (Mosalaganti *et al*, 2017). This residue is located in proximity of a prominent feature of the ROD β -propeller, the insertion of an α -helical hairpin (residue 168–190) between strands β 3C and β 3D (Fig 3B and Appendix Fig S2). The hairpin abuts against blade 2 of the propeller, partly bending it and increasing its separation from blade 3, and generating a deep, roughly cylindrical cavity between the two blades (Fig 3C). Leu120 lines the entry point of the cavity. AF2 predicts the C-terminal region of Spindly to interact with this region of the ROD β -propeller, and modeling the farnesyl group on Cys602 shows that the cavity is ideally dimensioned to receive the farnesyl group (Fig 3D–F).

The entire cavity is lined with hydrophobic residues, including Leu100, Leu108, Leu110, Leu119, Leu120, Phe124, Met153, Ile164, Leu167, Leu169, and Ile191, in addition to two polar residues, Asn122 and Ser193 (Fig 3E and F). To test the role of this pocket in the binding of farnesylated Spindly (Spindly^F), we tried to occlude it by generating two mutant RZZ complexes in which hydrophobic residues lining the farnesyl-binding pocket were replaced with bulkier ones (as described in the legend of Fig 3G). Confirming our hypothesis, the resulting mutants were stable but apparently unable to interact with Spindly^F in a size-exclusion chromatography experiment, contrarily to wild-type RZZ, with which Spindly^F formed a stoichiometric complex (Fig 3G).

AF2 also predicts that the Spindly chain, while reaching the farnesyl-binding pocket facing Cys602, aligns along a ridge on the side of the ROD β -propeller (Fig EV2A). To validate this binding

mode, we generated four Spindly mutants affecting three individual residues predicted to contact the ROD interface, Ile589, Ser594, and Thr600. To varying degrees, all four mutants impaired the interaction of Spindly with RZZ (Fig EV2B). This is consistent with the AF2 prediction that the interaction of Spindly with the RZZ complex is not limited to the farnesyl moiety and to immediately neighboring residues. Conversely, the mutations are not likely to affect *in vitro* farnesylation, as sequence requirements for the farnesylation reaction are largely limited to the C-terminal CAAX motif (Moore *et al*, 1991; Reid *et al*, 2004; Maurer-Stroh & Eisenhaber, 2005).

The *C. elegans* and *D. melanogaster* Spindly sequences have no C-terminal cysteine for isoprenylation (Holland *et al*, 2015). Analysis of ROD sequences in these organisms demonstrates differences predicted to ablate the hydrophobic farnesyl-binding cavity observed in human ROD. Specifically, in both species, the first of the two α -helices in the α -helical hairpin insertion that contributes to the architecture of the farnesyl-binding cavity is shorter by 3 residues (Appendix Fig S2). AF2 predicts that this causes a rotation of the second α -helix, positioning the side chain of Met184 (CeROD) precisely in the center of the cavity, obstructing it and making it inviable for farnesyl binding (Fig EV2C–F).

MPS1 nucleates RZZs fibers

The requirements for corona expansion remain incompletely characterized. For instance, the deletion of the ROD-1 β -propeller (residues 1–372) promotes ectopic filament formation in *C. elegans* embryos, while the equivalent deletion (residues 1–375) prevents expansion in human cells (Gama *et al*, 2017; Pereira *et al*, 2018). *In vitro*, a complex of CeZW10 (CZW-1) and CeROD with a deleted N-terminal propeller assembles a polymeric filamentous structure, whereas a full-length ternary complex is unable to polymerize (Pereira *et al*, 2018). Conversely, *in vitro* filament assembly of human RZZ, elicited by mild heating, requires Spindly^F (Sacristan *et al*, 2018). Furthermore, an N-terminal deletion removing 65 residues of Spindly promotes ectopic filament assembly in human cells even when Spindly is not farnesylated, an otherwise necessary condition for RZZ:Spindly binding and corona assembly (Sacristan *et al*, 2018).

To shed light on the corona assembly mechanism, we set out to dissect it *in vitro* with purified components. Using a spinning disk confocal microscope, we monitored polymerization of fluorescent

Figure 3. Farnesyl-binding pocket in the ROD propeller.

- Schematic representation of HsSpindly. The position of a CC1 box (red) and of the Spindly box (green) required for binding dynein:dynactin is shown, together with the position of relevant predicted coiled-coil regions.
- Cartoon representation of the 7-bladed ROD β -propeller (indicated as blades 1–7) modeled with AF2. The positions of blade 2, blade 3, and an α -helical hairpin representing an insertion between strands β 3c and β 3d are indicated. The four strands of each blade are indicated as A–D, with A and D being the innermost and outermost strands. The circle represents the entry point of the farnesyl-binding pocket.
- Surface representation of the ROD β -propeller. The circle is in the same position shown in panel B. The position of Leu120 is shown in yellow. This residue was targeted by photoactivatable cross-linker groups introduced in the farnesyl group attached to Cys602 of Spindly (Mosalaganti *et al*, 2017).
- The position of a modeled peptide corresponding to the C-terminal region of Spindly as predicted by AlphaFold2 (Jumper *et al*, 2021; Tunyasuvunakool *et al*, 2021) with a farnesyl moiety modeled on Cys602.
- A farnesyl moiety, shown in cyan spheres together with a few C-terminal residues of a modeled Spindly peptide, fitted snugly into a pocket lined exclusively by the side chains of several hydrophobic residues.
- Size-exclusion chromatography profiles and corresponding SDS–PAGE of the indicated samples. Two mutant RZZ complexes containing mutations in ROD L110F–L119F–L120K or L191M are indicated respectively as FFK and I/M. Note that in the bottom SDS–PAGE, the first and second lane were deliberately inverted and contain the first eluted fraction and the molecular weight marker. For all other shown SDS–PAGE, the marker precedes the first fraction.

Source data are available online for this figure.

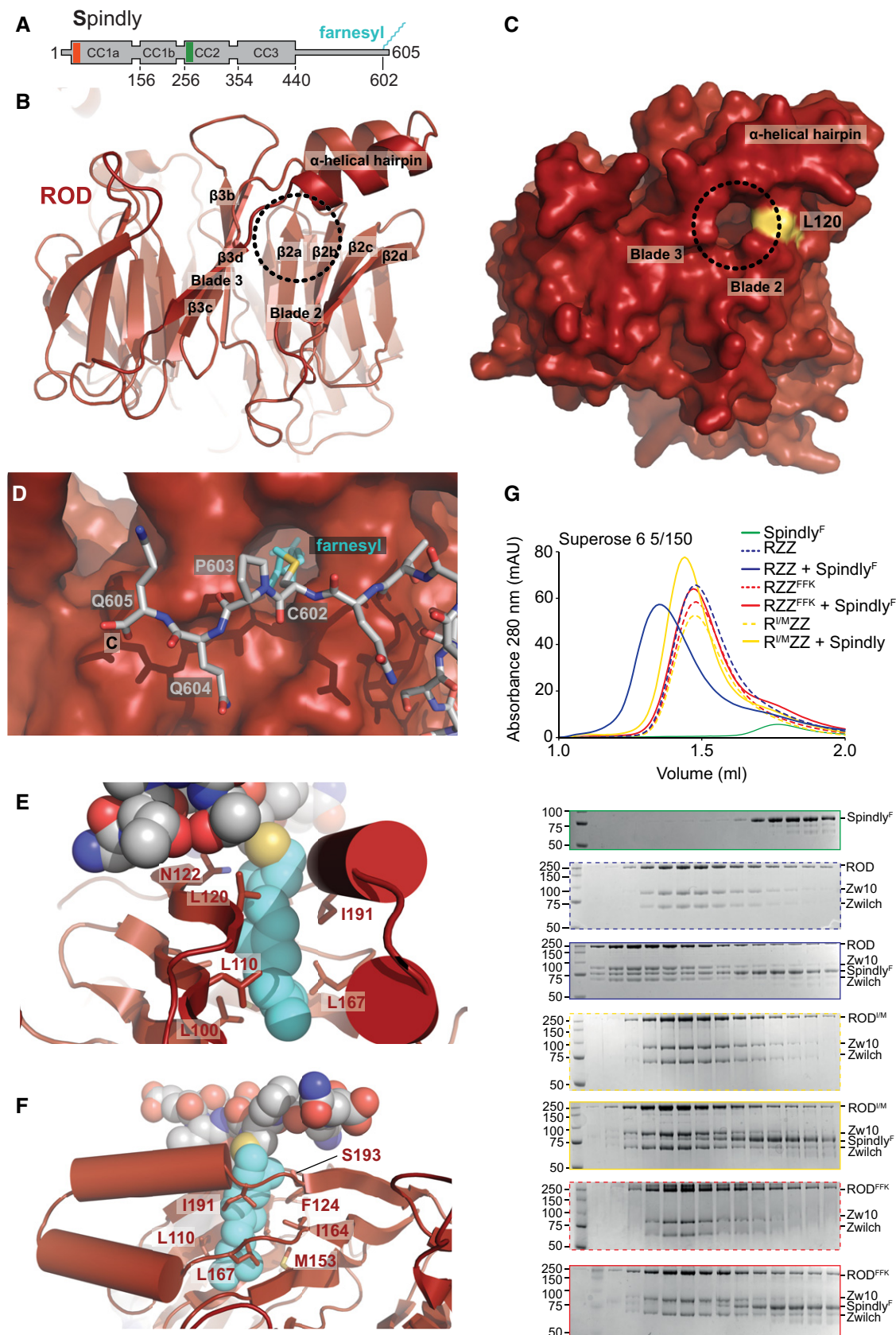


Figure 3.

mCherry-tagged RZZ or RZZS^F under various conditions after their purification to homogeneity and thorough dephosphorylation. At 20°C, neither mChRZZ nor mChRZZS^F (at a concentration of 4 μM) formed visible polymers. Conversely, and in agreement with our previous observations (Sacristan *et al*, 2018), incubation of mChRZZS^F for 1 h at 30°C promoted formation of copious fibers (Figs 4A and EV3A). No fibers were observed with mChRZZ or mChSpindly^F (Fig 4A), indicating that Spindly^F is required for fiber formation.

Previous studies identified a role of the MPS1 kinase, a central SAC component, in corona expansion in human cells (Rodriguez-Rodriguez *et al*, 2018; Sacristan *et al*, 2018). Regulatory effects of phosphorylation of corona components by additional mitotic kinases have also been reported (Pereira *et al*, 2018; Rodriguez-Rodriguez *et al*, 2018; Sacristan *et al*, 2018; Allan *et al*, 2020; Barbosa *et al*, 2020). We therefore asked whether mitotic kinases influenced corona assembly in our assay *in vitro*. When subjected to substoichiometric concentrations (typically 1/4 kinase/substrate ratio) of various mitotic kinases *in vitro* at 20°C in the presence of ATP, mChRZZS^F sample was phosphorylated by MPS1 on ROD, and by CDK1:cyclin B and to a minor extent by BUB1 on Spindly^F (as visualized by staining with the Pro-QTM Diamond Gel Staining Reagent; Fig 4B).

In line with a role of MPS1 phosphorylation of ROD in corona assembly (Rodriguez-Rodriguez *et al*, 2018; Sacristan *et al*, 2018), addition of MPS1 and ATP promoted spontaneous assembly of fibers at 20°C, an effect that was eliminated in the presence of reversine, an MPS1 inhibitor (Santaguida *et al*, 2010). Conversely, PLK1, Aurora B, BUB1, and CDK1:cyclin B did not promote fiber assembly, even when combined (Fig 4C). Subjecting mChRZZ or Spindly^F to MPS1 phosphorylation before mixing them to form a complex showed that only ROD needs to be phosphorylated for fibers to assemble (Fig EV3B and C). Spindly required farnesylation for filamentation because a C602A mutant failed to filament (Fig EV3D).

To corroborate these results in an *in vivo* setting, we released HeLa cells from a G2-phase arrest into mitosis in the presence of nocodazole and reversine to depolymerize microtubules and inhibit MPS1, respectively. MPS1 inhibition by reversine was confirmed by severe reduction of BUB1 kinetochore levels (Fig EV3E and F), as reported previously (Santaguida *et al*, 2010). Both Zwilch and Spindly decorated kinetochores when MPS1 was inhibited, albeit at a slightly reduced level in comparison with the control condition in the absence of MPS1 inhibitors (Fig 4D and E, quantified in Fig 4F). These effects of reversine on RZZ and Spindly recruitment are entirely consistent with a recent report (Rodriguez-Rodriguez *et al*, 2018) but milder than we had reported previously (Santaguida *et al*, 2010), arguably a consequence of improved experimental conditions and quantification procedures. Corona expansion was clearly completely inhibited in the presence of reversine, because Zwilch and Spindly showed the same dotted appearance of inner kinetochore markers instead of the crescent-like appearance observed in control cells (Fig 4D and E).

Next, we asked whether Spindly is necessary for corona expansion as predicted by our results *in vitro*. After depleting Spindly by RNAi (Fig 4G and H), we detected CENP-E and Zwilch at reduced but still highly significant levels on kinetochores of nocodazole-arrested mitotic cells. As for MPS1 inhibition, however, also in this case we observed an essentially complete failure to expand the corona (Fig 4I and J). Thus, neither Spindly nor MPS1 phosphorylation is strictly required for RZZ recruitment to the kinetochore. However, both are indispensable for expanding the corona.

Thus, the *in vitro* corona assembly assay we describe is an excellent predictor of cellular events at the corona, and leads to conclude that the presence of RZZ, Spindly, and active MPS1 is necessary to promote assembly of the corona at the kinetochore. Because corona assembly is limited to kinetochores, however, there must be additional signals to enrich the corona constituents to these subcellular compartments. When added to mitotic cells with an already-formed

Figure 4. MPS1 and Spindly promote corona assembly.

- A Confocal fluorescence microscopy-based filamentation assay at 561 nm shows mChRZZS^F (4 μM), but not mChRZZ (4 μM) or mChS^F (4 μM) as controls, forms filaments at 30°C. Scale bar: 5 μm. Two technical replicates were performed.
- B Coomassie and Pro-Q Diamond-stained gels on mChRZZS^F (4 μM) treated with the indicated kinases (1 μM) for 15 h at 20°C. Rev = reversine, used at 10 μM. These were precisely the samples studied in experiments in panel C.
- C A filamentation assay as in A demonstrates sufficiency of MPS1 phosphorylation for filamentation. Experiments for panels B and C were technically replicated three times.
- D Levels of Zwilch at kinetochores of HeLa cells that had been previously synchronized in G2 phase with 9 μM RO3306 for 16 h and then released into mitosis. Subsequently, cells were immediately treated with 500 nM reversine, 3.3 μM nocodazole, and 10 μM MG132 for 1 h and imaged while in mitosis. CREST serum was used to visualize kinetochores and DAPI to stain DNA. Scale bar: 10 μm. Three biological replicates were performed.
- E Cells treated as for panel D were treated for visualization of Spindly. Scale bar: 10 μm.
- F Scatter dot plots representing normalized total area of the Zwilch and Spindly signals, normalized to the reversine-untreated control, in the indicated number of cells from the experiment shown in panels C-D. Red lines indicate mean and standard deviation. Statistical analysis was performed with a nonparametric t-test comparing two unpaired groups (Mann-Whitney test). Symbols indicate n.s.P > 0.05, *P ≤ 0.05, **P ≤ 0.01, ***P ≤ 0.001, and ****P ≤ 0.000.
- G Representative images showing the effects of a knockdown of the endogenous Spindly in HeLa cells. RNAi treatment was performed for 48 h with 50 nM siRNA. Before fixation, cells were synchronized in G2 phase with 9 μM RO3306 for 16 h and then released into mitosis. Subsequently, cells were immediately treated with 3.3 μM nocodazole for an additional hour. CREST serum was used to visualize kinetochores and DAPI to stain DNA. Scale bar: 10 μm. Three biological replicates were performed.
- H Scatter dot plots representing normalized intensity ratios of Spindly over CREST for individual kinetochores of cells from the experiment shown in panel G. Red lines indicate median with interquartile range.
- I Levels of CENP-E and Zwilch were assessed in control cells and in cells treated as in panel G to knockdown Spindly. Three biological replicates were performed.
- J Scatter dot plots representing normalized total area of the CENP-E and Zwilch signals, normalized to the RNAi negative control, in the indicated number of cells from the experiment shown in panel I. Red lines indicate mean and standard deviation. Statistical analysis was performed with a nonparametric t-test comparing two unpaired groups (Mann-Whitney test). Symbols indicate n.s.P > 0.05, *P ≤ 0.05, **P ≤ 0.01, ***P ≤ 0.001, and ****P ≤ 0.000.

Source data are available online for this figure.

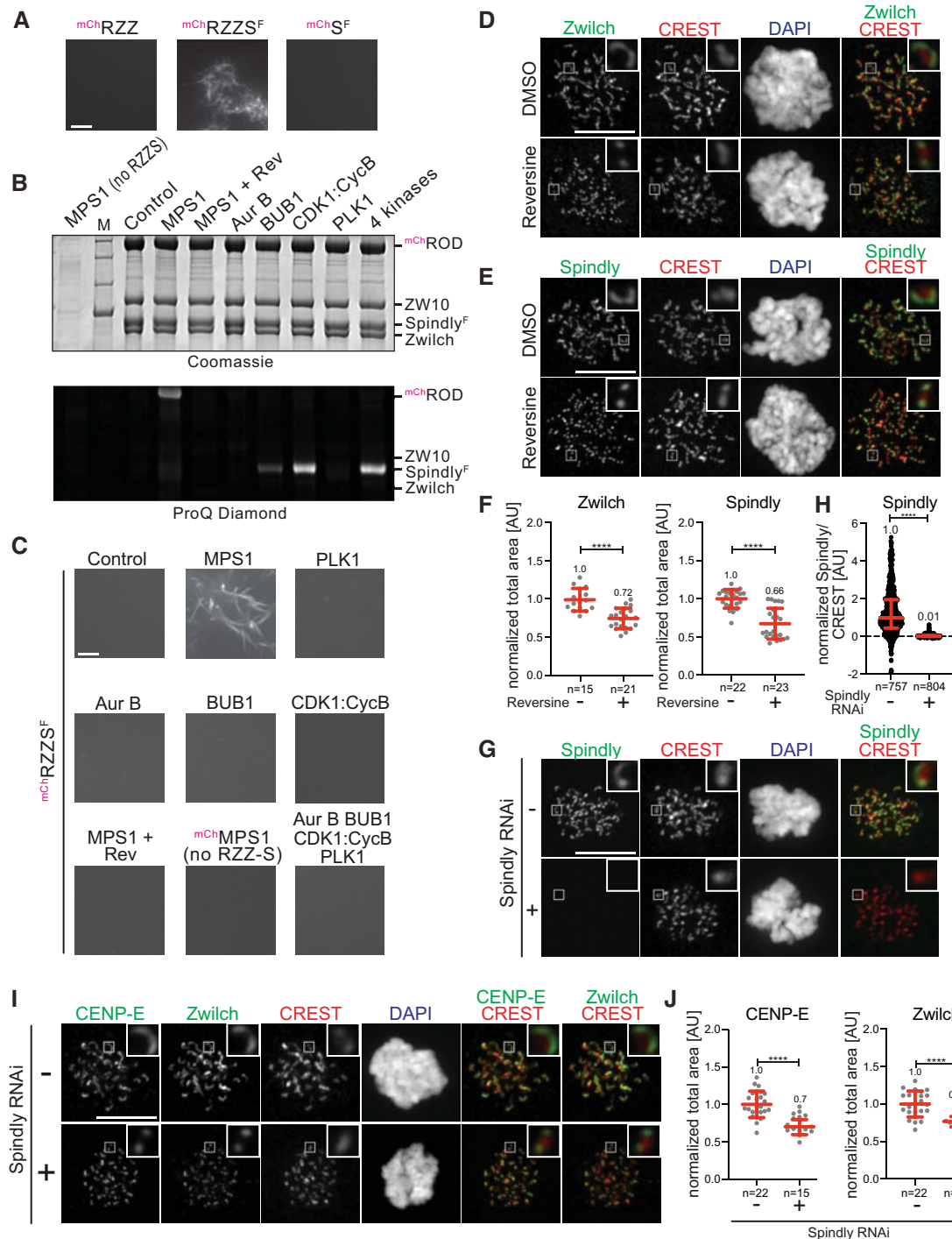


Figure 4.

corona, the selective cyclin-dependent kinase 1 (CDK1) inhibitor RO3306 (Vassilev *et al*, 2006) promoted corona detachment from the kinetochore, but no corona disassembly, as described previously (Pereira *et al*, 2018; Sacristan *et al*, 2018) (Fig EV3G). Conversely, the selective Aurora B kinase inhibitor hesperadin (Hauf *et al*, 2003) largely erased the recruitment of both RZZ (and therefore Spindly) and CENP-E to the kinetochore (Fig EV3H and I). Thus, both CDK1 and Aurora B are essential for directing or retaining the corona to

the kinetochore, but our results *in vitro* strongly suggest that they do so on the kinetochore side of the binding interface for the corona.

The role of MPS1 phosphorylation

The ROD β -propeller begins with the β 7d strand around residue Leu30 (Fig 5A and B). Thr13 and Ser15 of ROD, in the N-terminal

extension that precedes this point of entry into the β -propeller, were previously identified as MPS1 substrates required for corona assembly (Rodriguez-Rodriguez *et al*, 2018). These residues cannot be mapped with certainty in the reconstruction, due to its limited resolution in this peripheral region. However, AF2 predicts that the N-terminal region first augments blade 7 of the ROD β -propeller with an additional β -strand (β 7e), external to the outermost β 7d of the 4-strand propeller; then, after forming a helical turn that packs against the top part of blade 7, it also augments blade 6 with a short β 6e strand that pairs with β 6d, before finally entering the β -propeller (Fig 5A).

In agreement with the previous results, we found that a $^{\text{mCh}}\text{RZZS}^{\text{F}}$ mutant complex where $\text{ROD}^{\text{Thr13}}$ and $\text{ROD}^{\text{Ser15}}$ were mutated to alanine (T13A/S15A) did not assemble fibers (Fig 5C). The phosphomimetic mutant T13E/S15E, on the contrary, allowed $^{\text{mCh}}\text{RZZS}^{\text{F}}$ to form fibers at 20°C, even in the presence of reversine to abrogate MPS1 activity (Figs 5C and EV4A and B). The T13E/S15E mutant, however, failed to form fibers when Spindly^F was omitted (Fig EV4B). This confirms that Spindly^F is necessary for fiber formation even after bypassing MPS1 activity. Collectively, these results confirm that our fiber formation assay *in vitro* recapitulates crucial aspects of corona assembly.

The inability of the T13A/S15A mutant of $^{\text{mCh}}\text{RZZS}^{\text{F}}$ to form fibers was bypassed by mildly heating the sample to 30°C (Fig EV4A). Similarly, $^{\text{mCh}}\text{RZZS}^{\text{F}}$ complexes containing 15- or 26-residue N-terminal deletions in ROD ($^{\text{mCh}}\text{ROD}^{\Delta 15}$ and $^{\text{mCh}}\text{ROD}^{\Delta 26}$) were insensitive to MPS1 phosphorylation, but, like the T13A/S15A mutant, formed fibers when heat-treated (Fig 5D). Thus, the N-terminal region of ROD preceding the β -propeller is not strictly required for filament assembly, but its phosphorylation on Thr13 and Ser15 by MPS1 may overcome an existing nucleation barrier to filament assembly. To test this idea, we reasoned that if MPS1 phosphorylation of ROD were exclusively required to promote nucleation of $^{\text{mCh}}\text{RZZS}^{\text{F}}$ filaments, the stability of already-formed filaments would remain unaffected after ROD dephosphorylation. Indeed, successful dephosphorylation of $^{\text{mCh}}\text{RZZS}^{\text{F}}$ filaments with lambda phosphatase (Fig 5E) did not visibly interfere with filament number or stability (Fig 5F).

Zwilch contributes directly to fiber assembly

Previous studies implicated two highly conserved Zwilch residues, Glu422 and Asp426, in corona expansion in humans and nematodes (Gama *et al*, 2017; Pereira *et al*, 2018). To assess whether these residues also have a direct effect on corona assembly *in vitro*, we engineered a $^{\text{mCh}}\text{RZZS}^{\text{F}}$ complex containing alanine mutants of these residues (E422A/D426A). The E422A/D426A mutant complex failed to form fibers, both upon MPS1 phosphorylation and upon heating (Fig 5G). This was not caused by an impairment of the interaction of RZZ with Spindly, as the latter was unperturbed (Fig EV4C). Thus, Zwilch contributes directly to fiber assembly. The two conserved Zwilch residues are solvent-exposed and are part of a continuous face of the RZZ complex that also comprises blade 6 of the ROD β -propeller and the N-terminal region of ZW10 (Fig 5H), suggestive of an extensive interaction interface for corona expansion.

The RZZS polymers

To shed further light into the polymerization mechanism, we used negative-stain EM to visualize the $^{\text{mCh}}\text{RZZS}^{\text{F}}$ fibers obtained after mild heating or incubation with MPS1 kinase. Under either condition, the fibers appeared as flat sheets, consisting of somewhat irregular filaments packing side-a-side. The sheets coexisted with unpolymerized complexes and with small oligomers (Fig 6A). Essentially, identical sheets were obtained with a complex containing untagged ROD (RZZS^{F} , Fig EV5A) or with complexes expressing the ROD mutants T13A/S15A, T13E/S15E, and $\Delta 15$ (Fig EV5B). The sheets were not sufficiently ordered for a successful application of cryo-EM reconstruction methods.

Polymerization attempts with an RZZS complex where Spindly was also tagged with an N-terminal mCherry moiety ($^{\text{mCh}}\text{RZZ}/^{\text{mCh}}\text{S}^{\text{F}}$) prevented formation of fibers and rather promoted formation of complete rings, or of segments thereof of comparable curvature (Fig 6B), and regardless of whether initiated by heat or MPS1. Essentially, identical figures were also observed with an equivalent complex containing GFP-tagged Spindly ($^{\text{mCh}}\text{RZZ}/^{\text{GFP}}\text{S}^{\text{F}}$;

Figure 5. Role of the ROD N-terminal region in filamentation.

- A predicted N-terminal extension (green) of the ROD β -propeller (red), slightly rotated from the view in B. The propeller begins with strand β 7d and ends with strand β 7c, which leads into the helical domain. The N-terminal extension augments the sixth and seventh blades with external β -strands (β 6e and β 7e). The position of T13 and S15 on the extension is shown.
- The AF2 model confidence score (pLDDT, displayed blue to red through green from highly to poorly reliable) highlights regions of the model predicted with high or poor confidence (Jumper *et al*, 2021; Tunyasuvunakool *et al*, 2021).
- MPS1-induced filamentation experiments demonstrate that the phosphomimetic T13E/S15E ROD mutant bypasses the filamentation blockade induced by the MPS1 inhibitor reversine. The T13A/S15A mutant prevents MPS1-induced filamentation altogether. These experiments are also displayed in Fig EV4A.
- N-terminal deletion mutant of ROD ($\Delta 15$ and $\Delta 26$) removing the first 15 or 26 N-terminal residues that include the MPS1 phosphorylation sites Thr13 and Ser15 is unable to form filaments in the presence of MPS1 at 20°C, but can form filaments upon mildly heating to 30°C.
- The phosphorylation state of RZZ and Spindly^F was monitored by Pro-Q Diamond after SDS-PAGE separation of reactions.
- Filamentation assays with the indicated combinations of 8 μM $^{\text{mCh}}\text{RZZS}^{\text{F}}$, MPS1 (1 μM), and lambda phosphatase (0.4 mg/ml) in the presence of 10 μM reversine. Dephosphorylation reactions were carried out on already-formed filaments (see Methods). Samples were imaged by confocal microscopy. Dephosphorylation does not dissolve already-formed filaments.
- RZZ and RZZS complexes were reconstituted with the Zwilch^{E422A/D426A} mutant and tested for filamentation at 20°C in the presence of MPS1 or upon mildly heating to 30°C.
- Surface representation of the RZZ model depicting the position of Zwilch^{E422} and Zwilch^{D426} (in purple) and the positions of the ROD N-terminal region (green) and the highly conserved ZW10 N-terminus.

Data information: Scale bars in panels C, D, F, G = 5 μm . Two technical replicates for panels C, E, F, and G were performed. Three technical replicates for panel D were performed.

Source data are available online for this figure.

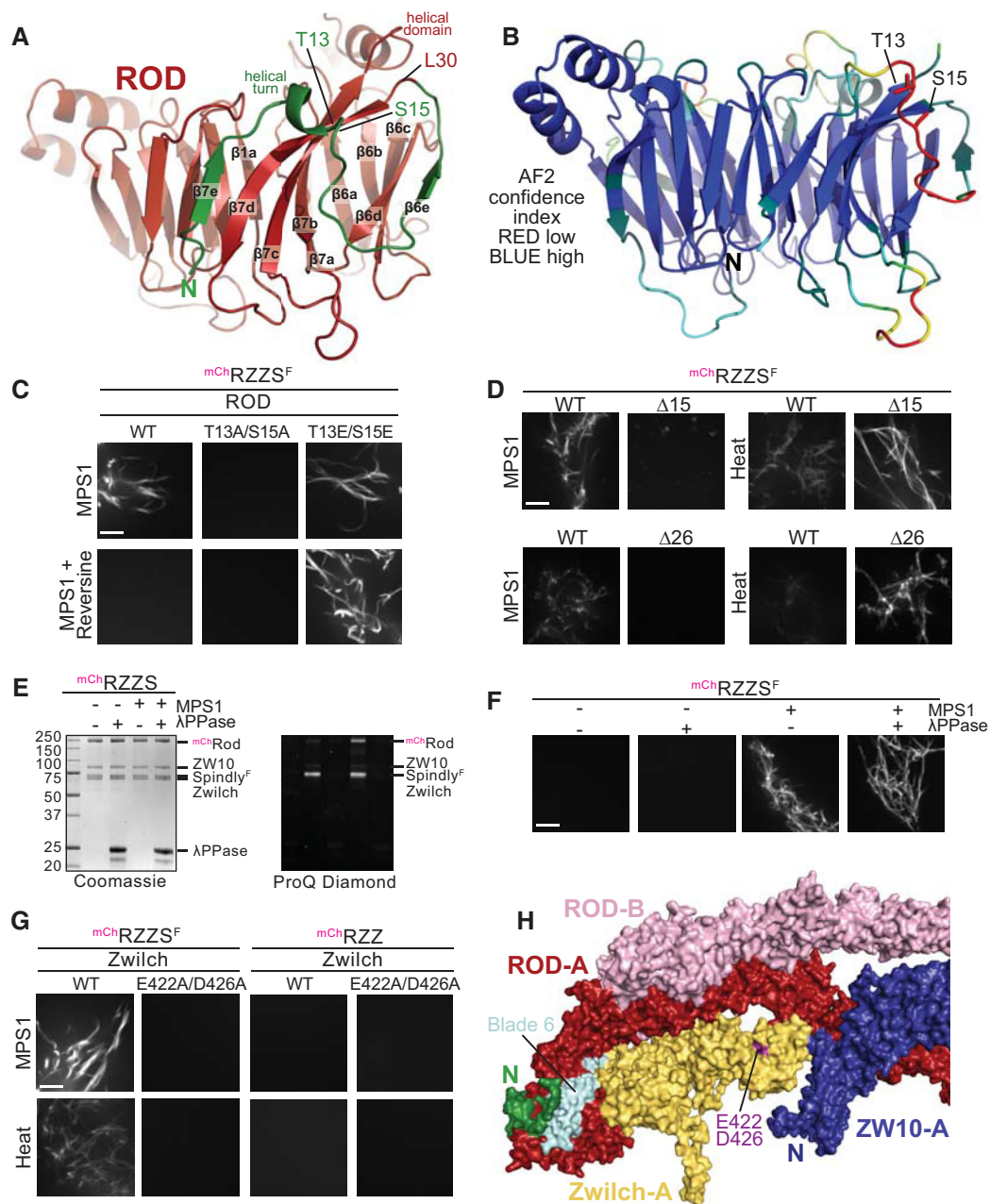


Figure 5.

Fig EV5C), even with untagged ROD (RZZ/^{GFP}S^F; Fig 6C). Cleavage of the GFP moiety from the latter construct after polymerization into rings promoted the lateral association of the filamentous rings into bundled rings, with a texture that was considerably less dense than that of the sheets, suggesting that bundles of rings do not pack as tightly as bundles of filaments in the sheets (Fig 6C).

Thus, N-terminal tagging of Spindly promotes the assembly of rings or curved filaments, likely because it inhibits “lateral” interaction of RZZS protomers that enables the formation of sheets. The curvature of the rings, whose average diameter is approximately 0.65 μ m (Fig 6D), is remarkably similar to the curvature of kinetochore

crests when the corona expands (Magidson *et al*, 2015) (Fig EV5D). Two-dimensional (2D) class averages of short segments of the negatively stained samples comprising a few consecutive ring subunits revealed a substantial orientation preference that ultimately prevented the successful calculation of a 3D reconstruction (Fig EV5E). Similar analyses using the rare rings observed at cryogenic temperatures suffered from the same extreme orientation preferences and were unsuitable for coherent reconstructions (Fig EV5F). Nonetheless, these analyses revealed that the rings appear to have a period of approximately half of the RZZ length (\approx 23 nm) and a width comparable to that of the RZZ (\approx 11 nm)

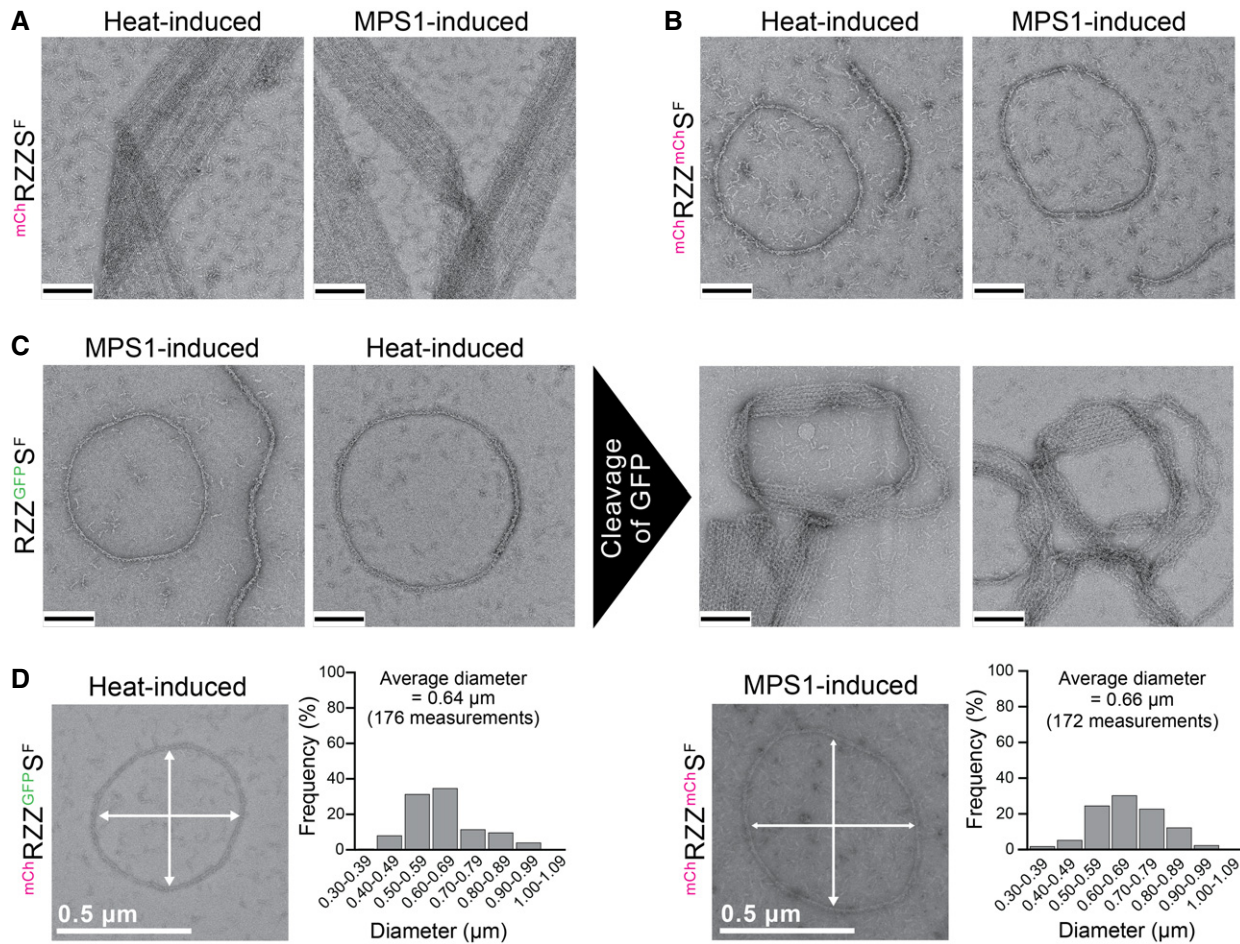


Figure 6. Ultrastructural analysis of RZZS sheets and filaments.

A Negative-stain electron microscopy analysis of heat- and MPS1-induced sheets of filament of farnesylated ^{mCh}RZZS. Scale bar (black): 200 nm.
B ^{mCh}RZZ^{mChS} forms rings and curved single filaments rather than sheets. Scale bar: 200 nm.
C The GFP of Spindly was removed with PreScission protease, and the resulting objects were imaged by negative-stain EM. Scale bar: 200 nm.
D Heat-induced ^{mCh}RZZ^{GFP SF} and MPS1-induced rings of ^{mCh}RZZ^{mChS} have similar diameters. As shown in panel B, heat- and MPS1-induced rings of ^{mCh}RZZ^{mChS} also have very similar dimensions.

Data information: Experiments in panels A-C were technically replicated at least three times. Experiments in D were carried out once.

(Fig EV5G), suggesting that they form through staggering of individual RZZS complexes.

The role of Spindly

To shed light on how Spindly promotes corona assembly, we investigated the corona assembly propensity of various Spindly deletion mutants, including Spindly^{250-C} and Spindly^{354-C}, where the CC1a/b segment of Spindly (250-C) or the CC1a/b and CC2 segments (354-C) are deleted, respectively (Fig 3A). Both Spindly constructs, upon farnesylation, interacted with the RZZ complex in size-exclusion chromatography experiments (Fig 7A). Conversely, a further deletion construct, Spindly^{440-C}, was unable to interact with the RZZ complex.

While Spindly^{250-C} supported corona expansion *in vitro* upon MPS1 phosphorylation and mild heating, indistinguishably from

full-length Spindly, Spindly^{354-C} did not support corona assembly (Fig 7B and Appendix Fig S3A). Furthermore, while Spindly^{354-C} bound the RZZ *in vitro*, it was unable to decorate kinetochores after introduction by electroporation into HeLa cells depleted of endogenous Spindly (Fig 7C and D, quantified in panel E). As expected, therefore, there was no expansion of the corona in these cells, as shown by the dot-like appearance of CENP-E, contrasting its crescent-like appearance observed in control cells with a well-formed corona. Spindly decorates kinetochores even when corona expansion is suppressed with an MPS1 inhibitor (Fig 4E), indicating that its localization to kinetochores is not contingent on corona expansion. Thus, failure of Spindly^{354-C} to reach kinetochores is unlikely to reflect its inability to assemble the corona (Fig 7C). Rather, Spindly^{354-C} may bind RZZ with reduced affinity or may be unable to interact with one or more additional kinetochore receptors ultimately required to stabilize the RZZS complex.

Collectively, these results indicate that a segment of Spindly encompassing residues 250–353 contains a critical determinant of corona assembly and kinetochore recruitment, possibly distinct or even overlapping. To shed further light on this question, we took advantage of our previous observation that Spindly^{1–275} and Spindly^{306–C} are stable Spindly constructs (Mosalaganti *et al*, 2017; Sacristan *et al*, 2018) to build a new deletion mutant, Spindly^{A276–306}. Spindly^{A276–306} bound robustly to the RZZ complex in size-exclusion chromatography experiments (Appendix Fig S3B), but was unable to support corona expansion *in vitro* (Fig 7B) and failed to reach the kinetochore (Fig 7F, quantified in panel G; note that the very modest mCherry signal shown to overlap with the centromere and inner kinetochore is a localization artifact of the mCherry tag). In conclusion, these results identify a segment comprising 31 residues of Spindly (276–306) as a crucial determinant of Spindly kinetochore localization and corona expansion.

Discussion

The high-resolution cryo-EM structure of the RZZ complex reported here crowns a succession of studies that began with the biochemical reconstitution and bioinformatic analysis of RZZ subunits, the determination of the crystal structure of Zwilch, and the report of a low-resolution EM reconstruction of the RZZ (Civril *et al*, 2010; Altenfeld *et al*, 2015; Mosalaganti *et al*, 2017). Our new structural analysis leveraged a pipeline that combined experimental structure determination using cryo-EM, model building based on experimental 3D reconstructions, and the enhanced prediction capabilities of AlphaFold2 (Jumper *et al*, 2021; Tunyasuvunakool *et al*, 2021), which were instrumental for model building in more peripheral regions of the reconstruction where the local resolution did not allow *de novo* model building. Collectively, this pipeline allowed us to reveal the structure of the RZZ complex at near-atomic resolution. The new structure explains how intermolecular interactions of the subunits promote the assembly of the RZZ complex; it also explains how RZZ interacts with the farnesyl moiety of Spindly; finally, it sets the basis for understanding how RZZ assembles into supramolecular structures in the corona.

We refined an *in vitro* assay for corona reconstitution that allowed us to probe several aspects of the polymerization reaction. First, we demonstrate that RZZS oligomerization *in vitro* into flat sheets or rings is kinetically controlled, and can be induced either by raising the temperature or by addition of the MPS1 kinase. Under all tested conditions, RZZ polymerization *in vitro* required Spindly^F, implicating it as a crucial building block of the corona. Two non-mutually exclusive possibilities are that Spindly^F contributes directly to binding interfaces required for polymerization or that it induces a conformational change in the RZZ required for polymerization. Our initial efforts to reveal the structure of the RZZS^F filament were thwarted by the limited order of the fibers we have obtained and by a very limited number of orientations on the EM grids. Future work will have to address this bottleneck, shedding light on the organization of the individual RZZS complex and of its polymeric form.

Nonetheless, our studies identified and mutationally probed several crucial interfaces for polymerization, including the N-terminal region of Spindly and a conserved acidic residue pair in Zwilch. Previous observations identified RZZ and Spindly as being both necessary for corona assembly in human cells (Rodriguez-Rodriguez *et al*, 2018; Sacristan *et al*, 2018). Our results *in vivo* are consistent with this tenet, but are further supported by polymerization experiments *in vitro* that showed a nearly perfect correlation with corona assembly in living cells. Human RZZS^F polymerizes efficiently at 30°C *in vitro* in the absence of a kinetochore support, whereas its polymerization in cells is seeded by the kinetochore and never extends far from it. While this may seem to suggest that other control mechanisms prevent RZZS oligomerization away from kinetochores, it should be considered that our experiments *in vitro* were carried out at RZZS^F concentrations (usually 4 μM) likely to be approximately two orders of magnitude higher than those existing in cells, as inferred by the fact that most SAC components have concentrations comprised between 10 and 100 nM (Simonetta *et al*, 2009). High concentration of building blocks likely facilitates polymerization, and indeed, RZZS^F filaments became sporadic or were not any longer observed at mid-nanomolar concentrations of RZZS^F (Appendix Fig S3C). Based on these observations, we suspect that the determinants of corona assembly, with the exclusion of an

Figure 7. Influence of Spindly on corona assembly and kinetochore recruitment.

- A Size-exclusion chromatography and SDS–PAGE of elution fractions of the indicated samples. Each Spindly construct was incubated with RZZ in the absence (dotted lines) or in the presence (continuous lines) of farnesyl transferase and farnesyl pyrophosphate. Elution shifts of Spindly^F and of the resulting RZZS^F complexes is indicative of successful interaction. Two technical replicates were performed.
- B MPS1-induced filamentation experiments on the indicated mChRZZS^F complexes (4 μM, further diluted to 0.5 μM for imaging) using a confocal spinning disk fluorescence microscope at 561 nm. Scale bar: 5 μm. Two technical replicates were performed.
- C Schematic of the cell synchronization and imaging experiment shown in D. After electroporation, cells were allowed to recover for 8 h. Subsequently, cells were synchronized in G2 phase with 9 μM RO3306 for 15 h and then released into mitosis by inhibitor washout. Before fixation, cells were treated with 3.3 μM nocodazole for 1 h.
- D Representative images of fixed HeLa cells electroporated with full-length mChSpindly and mChSpindly^{354–605} constructs in cells depleted of endogenous Spindly by RNAi. Spindly localization was detected with an antibody against the C-terminal region of Spindly. Corona expansion or lack thereof was monitored through CENP-E. CREST serum was used to visualize kinetochores, DAPI to stain for DNA. Scale bar: 10 μm. Experiments were replicated three times.
- E Scatter dot plots representing normalized intensity ratios of the indicated Spindly constructs over CREST for individual kinetochores of cells from the experiment shown in panel D. Red lines indicate median with interquartile range. Statistical analysis was performed with a nonparametric t-test comparing two unpaired groups (Mann–Whitney test). Symbols indicate n.s.P > 0.05, *P ≤ 0.05, **P ≤ 0.01, ***P ≤ 0.001, and ****P ≤ 0.000.
- F Cells treated like in C–D were electroporated with the indicated mChSpindly constructs. Corona expansion was evaluated through the appearance of Zwilch. Experiment replicated three times. Scale bar: 10 μm.
- G Kinetochore intensities were quantified like in panel E. Red lines indicate median with interquartile range. Statistical analysis was performed with a nonparametric t-test comparing two unpaired groups (Mann–Whitney test). Symbols indicate n.s.P > 0.05, *P ≤ 0.05, **P ≤ 0.01, ***P ≤ 0.001, and ****P ≤ 0.000.

Source data are available online for this figure.

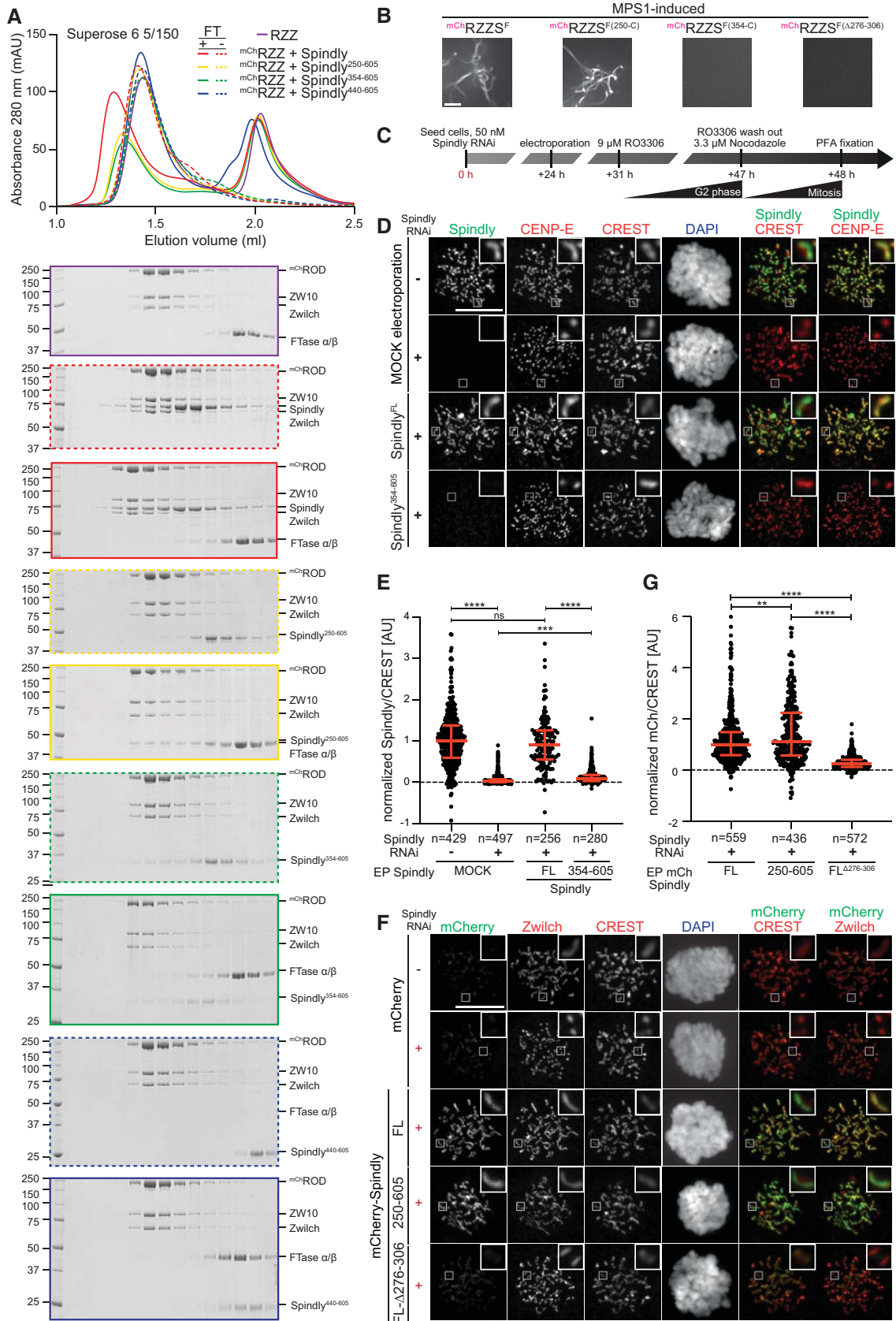


Figure 7.

unknown receptor site in the kinetochore, are entirely contained with the RZZS complex.

A crucial factor likely explaining why RZZS filaments form only at kinetochores is that RZZS polymerization appears to be kinetically controlled, with MPS1 phosphorylation acting as catalyst to remove a steric blockade to oligomerization involving the ROD N-terminal region. As kinetochores enrich MPS1 during mitosis, and MPS1 activity is highest at these structures, albeit not limited to them (Kuijt *et al*, 2020), polymerization may become naturally spatially limited to kinetochores. The release of ROD from an auto-inhibited state upon MPS1 phosphorylation, postulated here, should be considered alongside the proposed auto-inhibition of Spindly, shown to involve an intramolecular interaction of its coiled coils (Sacristan *et al*, 2018; preprint: d'Amico *et al*, 2022). It is remarkable that sequence determinants in the CC2 of Spindly, when deleted (Spindly^{Δ276-306}), not only prevent the intramolecular interaction with CC1a/b, filamentation *in vitro*, and ectopic filament formation (Sacristan *et al*, 2018; preprint: d'Amico *et al*, 2022), but also kinetochore recruitment. In a previous study, a deletion of residues 254–284 of Spindly was shown to retain kinetochore localization, whereas a deletion of the first 292 residues impaired kinetochore localization (Barisic *et al*, 2010). When taken collectively, the available information points to a handful of residues in Spindly, within the fragment 276–306 as being necessary for kinetochore recruitment. Release of Spindly auto-inhibition may be concomitant with the binding of the elusive kinetochore receptor(s). In conclusion, two regulatory mechanisms may act on different aspects of RZZS regulation at kinetochores, with MPS1 phosphorylation of ROD being predominantly implicated in corona expansion, and release of Spindly auto-inhibition being predominantly implicated in enabling binding of dynein and dynactin.

The mechanism of corona assembly bears similarities to the process of coat assembly that drives intracellular trafficking of membranous organelles. In addition to evident structural similarities, most notably of ROD with clathrin and COPs, which are also characterized by a succession of an N-terminal β -propeller and a C-terminal α -solenoid, both processes are spatially and kinetically controlled so that they occur only at defined cellular locales and in the presence of appropriate triggers (Arakel & Schwappach, 2018; Sigismund *et al*, 2021). The high-affinity binding site that drives RZZ recruitment to the kinetochore remains elusive, but appears to be confined within the KMN network (Miller *et al*, 2008; Chan *et al*, 2009; Pagliuca *et al*, 2009; Sundin *et al*, 2011; Varma *et al*, 2013; Caldas *et al*, 2015; Pereira *et al*, 2018).

At least two kinases, in addition to MPS1, are also required for assembly and/or retention of the corona, CDK1 and Aurora B. Acute inhibition of these kinases results respectively in the detachment of the assembled corona from the kinetochore (CDK1) and in the extensive depletion of corona components at kinetochores (Aurora B). In experiments with purified kinases *in vitro*, we did not find prominent Aurora B phosphorylation sites on the RZZS^F complex, suggesting that Aurora B does not control corona assembly directly. Because Aurora B is critically required for MPS1 recruitment to kinetochores (Santaguida *et al*, 2010; Nijenhuis *et al*, 2013), we suspect that Aurora B inhibition blocks the essential function of MPS1 as promoter of corona assembly. On the contrary, CDK1 phosphorylates Spindly^F efficiently *in vitro*, but without triggering filamentation. It is possible that the detachment of the corona after CDK1 inhibition reflects an

essential role of CDK1 phosphorylation of Spindly in its kinetochore recruitment (e.g., by creating a phospho-dependent binding site or conformational change). In this case, CDK1 inhibition may be recapitulated by expression of non-phosphorylatable mutants of Spindly. Alternatively, CDK1 may contribute to the generation of a binding site for the RZZS on the kinetochore.

Thus, the RZZS emerges from our study as being sufficient to assemble the corona. This conclusion also explains why depletion of additional corona components, including CENP-E, CENP-F, DD, and MAD1-MAD2, does not visibly disrupt corona assembly and RZZ kinetochore recruitment (Gassmann *et al*, 2010; Ciossani *et al*, 2018; Allan *et al*, 2020). These proteins, on the contrary, may retain residual kinetochore localization even after depletion of RZZS components. The MAD1-MAD2 complex, for instance, requires the RZZ complex for kinetochore localization, and will localize to the kinetochore even if the corona cannot expand due to Spindly depletion (Rodriguez-Rodriguez *et al*, 2018). In another example, CENP-E and CENP-F, in addition to interacting with the corona, have also been shown to interact with the non-corona components BUBR1 and BUB1, respectively (Ciossani *et al*, 2018; Raaijmakers *et al*, 2018; Legal *et al*, 2020). We anticipate that our corona assembly assay may shed light on the mechanism of recruitment of these additional corona components.

A fundamental unresolved question in kinetochore biology is how the conversion of microtubule attachments from lateral to end-on promotes corona stripping. Plausibly, this sudden transition reflects a weakening of the interaction of the RZZS with its kinetochore receptor, leading to DD-directed detachment of the corona from the kinetochore. What triggers this change in binding affinity, however, remains unclear. Our studies, by unveiling the molecular features of the RZZ complex and by defining requirements for its physical interactions, provide an initial step toward the elucidation of this very complex and important question.

Materials and Methods

Protein expression and purification

Expression and purification of Spindly and RZZ constructs were carried out essentially as previously described (Moslaganti *et al*, 2017; Sacristan *et al*, 2018). Proteins were expressed using the BiGBac recombinant expression system (Weissmann *et al*, 2016). Bacmid was produced from EMBAcY cells and used to transfect Sf9 cells to produce baculovirus. The baculovirus was subjected to three rounds of amplification and used to infect TnaO38 cells. Cells were cultured for 72 h before harvesting. A pellet from expression in 500 ml of TnaO38 cells was lysed by sonication in 100 ml lysis buffer (50 mM HEPES, pH 8.0, 250 mM NaCl, 2 mM TCEP, 50 mM imidazole) supplemented with 1 mM PMSF and protease inhibitor cocktail (Serva). The lysate was then cleared by centrifugation at 100,000 g for 45 min. The cleared lysate was loaded onto a HisPrep Fast Flow column (Cytiva) pre-equilibrated in lysis buffer, and washed with 500 ml lysis buffer, after which the bound protein was eluted with lysis buffer supplemented with 300 mM imidazole. The eluate was diluted 1:5 in Buffer A (50 mM HEPES, pH 8.0, 2 mM TCEP) and applied to a 6-ml Resource Q anion exchange column (Cytiva). The protein was then eluted using a 50–500 mM NaCl gradient. Peak

fractions were analyzed by SDS-PAGE, and those containing the relevant proteins were concentrated to 500 μ l volume, and subjected to size-exclusion chromatography on a Superdex S200 10/300 column (Cytiva) for Spindly, and on a Superose 6 10/300 for RZZ constructs, equilibrated in SEC buffer (50 mM HEPES, pH 8.0, 250 mM NaCl, 2 mM TCEP). Fractions were pooled and concentrated to 10 mg/ml, snap-frozen, and stored at -80°C until use. For dephosphorylation, 4 μM $^{\text{mCh}}$ RZZS^F complex or preformed MPS1-induced $^{\text{mCh}}$ RZZS^F polymers were incubated for 15 h in M-buffer at 20°C with or without 0.4 mg/ml Lambda phosphatase (produced in house), in presence of 10 μM reversine. Spindly ^{Δ 276–306} and Spindly C-terminal point mutants were expressed as mCherry fusions in *E. coli*. BL21-CodonPlus cells were transformed with a pET28a plasmid containing the coding sequence for the mCherry tag, a PreScission cleavage sequence, and the relevant construct, and grown in TB at 37°C to an OD₆₀₀ of 0.5. Expression was induced with 0.4 mM IPTG. The culture was then transferred into an incubator pre-cooled to 18 C, and grown overnight before harvesting. The pellet was then snap-frozen and stored at -80°C until purification. Untagged Spindly ^{Δ 276–306} was obtained by cleaving the mCherry tag with PreScission protease, by incubating 2 mg of mCherry-Spindly ^{Δ 276–306} with 0.1 mg of in-house produced PreScission protease overnight. The sample was then loaded on a Superose 6 column equilibrated in SEC buffer to remove the tag and PreScission protease. Fractions were then pooled and concentrated to 10 mg/ml, snap-frozen, and stored at -80°C until use.

Production of MPS1 kinase

An mCherry-MPS1-6His construct was generated by subcloning in a pLIB vector. The corresponding baculovirus was generated in Sf9 insect cells (Wickham *et al*, 1992). After three rounds of amplification (V0, V1, and V2, 4 days each), 100 ml of V2 was inoculated in 1 liter of Tnao38 cells. 24 h after infection for expression, reversine (Santaguida *et al*, 2010) was added to the growth medium (1 μM) to maximize expression yields. After 60 h of expression at 27°C , cells were pelleted, washed in PBS, pelleted again, and either stored at -80°C after flash-freezing in liquid nitrogen, or used directly for purification. Every purification step was performed on ice or at 4°C . The pellet was resuspended in \sim 100 ml buffer A (300 mM NaCl, 50 mM HEPES, pH 8, 5% glycerol, 2 mM TCEP, 10 mM imidazole, pH 8) and supplemented with PMSF (1:100), protease inhibitor mix HP Plus (1:500, Serva) and DNaseI (1:300, Roche), lysed by sonication, and cleared by centrifugation at 108,000 g for 45 min. The cleared lysate was applied to 5 ml Nickel-NTA (GE Healthcare) slurry beads previously equilibrated in buffer A and incubated on a rotating platform at 4°C for 2 h. The supernatant was removed by centrifugation (1,500 g , 5 min, 4°C), and the beads were washed with 100 ml buffer A. For the elution, the beads were incubated (\sim 15 min at 4°C) in 15 ml of buffer A supplemented with 300 mM imidazole, pH 8. Samples of the cleared lysate, of the supernatant, and of the elution were loaded on SDS-PAGE for analysis. The 15 ml elution was then concentrated, spun at max speed for 30 min in a bench-top centrifuge (at 4°C), and finally loaded on a Superdex 200 16/60 (GE Healthcare) previously equilibrated in MPS1 buffer (250 mM NaCl, 50 mM HEPES, pH 8, 5% glycerol, and 2 mM TCEP). The protein was then concentrated, aliquoted, and stored in -80°C after flash-freezing in liquid nitrogen.

In vitro farnesylation

Farnesyltransferase α/β mutant (W102T/Y154T) was expressed and purified as previously described (Mosalaganti *et al*, 2017). Spindly was diluted to 100 μM in farnesylation buffer (50 mM HEPES, pH 8.0, 250 mM NaCl, 10 mM MgCl₂, 2 mM TCEP), and farnesyltransferase was added to a final concentration of 30 μM . Farnesyl pyrophosphate (Sigma-Aldrich) was added stepwise to a final concentration of 300 μM . The reaction mixture was incubated at RT for 6 h, after which it was centrifuged at 16,000 g for 10 min to remove precipitate that formed during the reaction. The cleared reaction mixture was then loaded on a Superose 6 column equilibrated in SEC buffer to remove the farnesyltransferase. The fractions containing Spindly were identified by SDS-PAGE and pooled, concentrated to a final concentration of around 5 mg/ml, snap-frozen, and stored at -80°C until use.

Analytical size-exclusion chromatography

Analytical gel filtration runs were performed on Superose 6 Increase 5/150 columns (Cytiva) pre-equilibrated in SEC buffer. For runs with pre-farnesylated Spindly constructs, RZZ and Spindly were pre-incubated at a concentration of 2 μM and 6 μM , respectively, on ice for 1 h in SEC buffer. For runs with concurrent farnesylation, RZZ, Spindly, and FTase were incubated at a concentration of 5, 15, and 7.5 μM , respectively, for 2 h at room temperature in SEC buffer supplemented with 25 μM FPP, followed by 30 min on ice.

Filamentation experiments with RZZS or RZZ complexes

Heat-induced RZZS^F filaments were prepared by incubating 4 μM RZZ complex and 8 μM Spindly^F or 4 μM preassembled RZZS^F complex for 1 h at 30°C in H-buffer (50 mM HEPES, pH 7.5, 100 mM NaCl, 1 mM MgCl₂, and 1 mM TCEP). Tags were removed from $^{\text{mCh}}$ RZZ^{GFP}S^F filaments by incubating the polymers for 1 h at 30°C with 0.5 mg/ml PreScission protease (produced in-house). MPS1-induced filaments were obtained by incubating 4 μM RZZ complex and 8 μM Spindly^F or 4 μM RZZS^F preassembled purified complex for 15 h at 20°C in M-buffer (50 mM HEPES, pH 7.5, 100 mM NaCl, 1 mM MgCl₂, and 1 mM TCEP), supplemented with 2 mM ATP at pH 8.0 and in the presence of 1 μM MPS1. The effect of other mitotic kinases on RZZS^F complex filamentation was tested in the same conditions using 1 μM of purified protein kinase (produced in-house). Reversine (Cayman Chem.) was dissolved at 10 mM in DMSO and used at 10 μM final concentration. Protein phosphorylation was monitored by Pro-Q Diamond phosphostaining (Thermo Fisher Scientific) after SDS-PAGE separation. Independent MPS1 phosphorylation of RZZ and Spindly^F protein stocks was carried out by incubating 8 μM RZZ and 16 μM Spindly^F overnight in M-buffer at 20°C , supplemented with 2 mM ATP, pH 8.0, and 1 μM MPS1. For dephosphorylation experiments, polymers were incubated for 15 h in M-buffer at 20°C with or without 0.4 mg/ml lambda phosphatase (produced in-house), in the presence of 10 μM reversine.

Confocal imaging of RZZS^F filaments

Glass flow chambers of about 10 μl volume were assembled using standard cover glasses and glass slides, held together by double-

sided tape (Tesa). Heat- or MPS1-induced RZZS^F filaments were diluted to 0.5 μM in H- or M- buffer (see above), respectively, and imaged in the glass chambers, at room temperature using a spinning disk confocal device on the 3i Marianas system at 100 \times magnification. Sample images were acquired as 5-stacks of z-sections at 0.27 μm , converted into maximal intensity projections, exported, and processed with Fiji (Schindelin *et al*, 2012).

Cell culture and imaging

Cell culture and drug treatment

HeLa cells were grown in Dulbecco's modified Eagle's medium (DMEM; PAN Biotech) supplemented with 10% tetracycline-free FBS (PAN Biotech) and L-glutamine (PAN Biotech). Cells were grown at 37°C in the presence of 5% CO₂. Where indicated, nocodazole (Sigma) was used at 3.3 μM , RO3306 (Calbiochem) at 9 μM , MG132 (Calbiochem) at 10 μM , hesperadin at 500 nM (Merck), and reversine (Cayman Chem.) at 500 nM.

Cell transfection and electroporation

Depletion of endogenous Spindly was achieved through reverse transfection with 50 nM Spindly siRNA (5'-GAAAGGGUCUCAA ACUGAA-3' obtained from Sigma-Aldrich) for 48 h with RNAiMAX (Invitrogen, Carlsbad, California, USA). For rescue experiments, 24 h after Spindly depletion, we electroporated recombinant Spindly constructs, either unlabeled or labeled with an N-terminal mCherry, at a concentration of 7 μM in the electroporation slurry (as previously described in Alex *et al*, 2019) (Neon Transfection System, Thermo Fisher). Control cells were electroporated with mCherry or electroporation buffer, respectively. Following an 8-h recovery, cells were treated with 9 μM RO3306 (Calbiochem) for 15 h. Subsequently, cells were released into mitosis in the presence of 3.3 μM nocodazole (Sigma) for 1 h.

Immunofluorescence

Cells were grown on coverslips pre-coated with Poly-L-lysine (Sigma-Aldrich). Cells were pre-permeabilized with 0.5% Triton X-100 solution in PHEM (Pipes, HEPES, EGTA, MgCl₂) buffer supplemented with 100 nM microcystin for 5 min before fixation with 4% PFA in PHEM for 20 min. After blocking with 5% boiled goat serum (BGS) in PHEM buffer, cells were incubated for 2 h at room temperature with the following primary antibodies: BUB1 (mouse, Abcam, ab54893, 1:400), CENP-E (mouse, Abcam, ab5093, 1:200), Spindly (rabbit, Bethyl Laboratories, A301-354A, 1:1,000), Zwi1 (rabbit, made in-house, SI520, 1:900), and CREST/anti-centromere antibodies (Antibodies, Inc., 1:200) diluted in 2.5% BGS-PHEM supplemented with 0.1% Triton X-100. Subsequently, cells were incubated for 1 h at room temperature with the following secondary antibodies: goat anti-mouse Alexa Fluor 488 (Invitrogen A11001), donkey anti-rabbit Rhodamine Red (Jackson ImmunoResearch 711-295-152), donkey anti-rabbit Alexa Fluor 488 (Invitrogen A21206), and goat anti-human Alexa Fluor 647 (Invitrogen, Carlsbad, California, USA). All washing steps were performed with PHEM-T buffer. DNA was stained with 0.5 $\mu\text{g}/\text{ml}$ DAPI (Serva), and Mowiol (Calbiochem) was used as mounting media.

Cell imaging

Cells were imaged at room temperature using a spinning disk confocal device on the 3i Marianas system equipped with an Axio

Observer Z1 microscope (Zeiss), a CSU-X1 confocal scanner unit (Yokogawa Electric Corporation, Tokyo, Japan), 100 \times /1.4NA Oil Objectives (Zeiss), and Orca Flash 4.0 sCMOS Camera (Hamamatsu). Images were acquired as z-sections at 0.27 μm . Images were converted into maximal intensity projections, exported, and converted into 16-bit TIFF files. Automatic quantification of single kinetochore signals was performed using the software Fiji with background subtraction. Measurements were exported in Excel (Microsoft) and graphed with GraphPad Prism 9.0 (GraphPad Software). Statistical analysis was performed with a nonparametric *t*-test comparing two unpaired groups (Mann–Whitney test). Symbols indicate n.s. $P > 0.05$, * $P \leq 0.05$, ** $P \leq 0.01$, *** $P \leq 0.001$, and **** $P \leq 0.000$. The figures were arranged using the Adobe Illustrator 2022 software.

Negative-stain electron microscopy sample preparation and image analysis

4 μl of 20–100 nM RZZS^F filaments was deposited on freshly glow-discharged Formvar/Carbon (Quantifoil) film-supported copper grid Cu400 (Sigma-Aldrich) and incubated for 1 min. Once excess sample was blotted away with filter paper, the grids were washed two times with 10 μl of H- or M-buffer (Heat- or MPS1-induced filaments, respectively), then once with 10 μl of 0.75% (w/v) uranyl formate (Sigma-Aldrich). After staining with 10 μl of 0.75% (w/v) uranyl formate for 30 s, grids were blotted, dried, and visualized at 120 kV using a Tecnai Spirit equipped with a LaB₆ cathode and a 4,000 \times 4,000 CMOS detector F416 (TVIPS). Images were recorded at a nominal magnification of 21–42,000 \times . Single measurements of the diameter of RZZS^F circular polymers were performed by processing negative-stain EM images with Fiji (NIH). Values were exported in Excel (Microsoft) and graphed with GraphPad Prism 6.0 (GraphPad Software). 2D classification of mChRZZ^{GFP}S^F filaments was performed using ISAC (Yang *et al*, 2012) within SPHIRE (Moriya *et al*, 2017). 148 images were collected at a magnification of 42,000 \times resulting in 2.6 $\text{\AA}/\text{pixel}$. Straight filament sections were manually selected, and segments of 256 \times 256 pixel and an overlap of 115 pixel were extracted from those, resulting in 2,730 particles. Classification was performed with standard parameters, using a radius of 120 pixel and a maximum of 50 members per class.

Cryo-EM grid preparation and data acquisition

Grids were prepared using a Vitrobot Mark IV (Thermo Fisher Scientific) at 13°C and 100% humidity. 4 μl of RZZ at a concentration of 5 mg/ml and supplemented with 0.02% Triton was applied to glow-discharged Quantifoil R2/1 grids and excess liquid removed by blotting (3.5 s at blot force -3) before vitrification in liquid ethane. Cryo-EM data were acquired on a Titan Krios electron microscope (Thermo Fisher Scientific) equipped with a field emission gun. Two datasets with 1,968 and 5,794 movies, respectively, were recorded on a K3 camera (Gatan) operated in super-resolution mode at a nominal magnification of 105,000, resulting in a super-resolution pixel size of 0.45 \AA . A Bioquantum post-column energy filter (Gatan) was used for zero-loss filtration with an energy width of 15 eV. Total electron exposure of 59 and 60 $\text{e}^-/\text{\AA}^2$, respectively, was distributed over 60 frames. Data were collected using the automated data collection software EPU (Thermo Fisher Scientific), with

three exposures per hole and a set defocus range of -1.2 to -2.7 μm . Details of data acquisition parameters are found in Table EV1.

Cryo-EM data processing

On-the-fly data pre-processing, including correction of beam-induced motion and dose-weighting by MotionCor2 (Zheng *et al*, 2017), CTF parameter estimation using CTFFIND4 in movie mode (Rohou & Grigorieff, 2015), and particle picking using a custom neural network in SPHIRE-crYOLO (Wagner *et al*, 2019), was performed within TransSPHIRE (Stabrin *et al*, 2020). 74,836 fourfold binned particles with dimensions of 180×180 pixels were extracted from the first dataset using SPHIRE (Moriya *et al*, 2017), and used for 2D classification in ISAC. An initial model was calculated in RVIPER using 81 good 2D classes and by imposing C2 symmetry. Initial 3D reconstruction in MERIDIEN was performed using 49,656 twofold binned particles of the second dataset, which were assigned to well-defined 2D classes and also with imposed C2 symmetry, resulting in a 4.7 \AA 3D reconstruction. Recentered particles from all micrographs of the second dataset were used for training an improved neural network for SPHIRE-crYOLO. 191,979 particles were picked with this network on 7,718 micrographs of both datasets and extracted with twofold binning and a size of 300×300 pixels. An initial 3D refinement of this particle stack in RELION (Zivanov *et al*, 2019) resulted in a 4.9 \AA reconstruction. After several rounds of particle polishing and CTF refinement in RELION, reconstructions with overall nominal resolutions of 4.1 and 3.9 \AA were obtained using 3D refinement in RELION or non-uniform refinement in cryoSPARC (Punjani *et al*, 2017, 2020), respectively (Fig EV1A and B). Local resolution was calculated, and the reconstruction locally filtered, using cryoSPARC (Fig EV1C). As the global reconstructions displayed a strong resolution gradient from the center to the exterior parts of the molecule (Fig EV1C), indicative of continuous flexibility within the complex, we turned to a focused refinement strategy. For this, we generated two focused masks, one for the central and one for the exterior part of one asymmetric half of the molecule. Then, we symmetry-expanded the particle stack according to the C2 symmetry and performed focused local refinements in cryoSPARC that resulted in reconstructions of 3.7 and 4.8 \AA , respectively, for the central and the exterior masks (Fig EV1A). The maps were fitted to the original unmasked C2-symmetric map, and a composite map was created using the “vop maximum” command in Chimera (Pettersen *et al*, 2004).

Model building, validation, and fitting

The central part of RZZ was built *de novo* using the 3.9 \AA reconstruction from cryoSPARC non-uniform refinement. This map was subjected to automated model building using phenix.map_to_model (Lieschner *et al*, 2019). The resulting initial model, which comprised many α -helices in the central part of the particle, was manually improved and extended and the correct sequence assigned in Coot (Emsley *et al*, 2010), yielding a model comprising almost full-length ZW10 and the central part of ROD (residues 890–1,440). AlphaFold2 (AF2) (Jumper *et al*, 2021; Tunyasuvunakool *et al*, 2021) was used in the original implementation, as well as in the modified “ColabFold” (preprint: Mirdita *et al*, 2021) and in the

“multimer” versions (preprint: Evans *et al*, 2021) to model subcomplexes of RZZ, specifically, the central region of ROD with ZW10, the “hook” region consisting of the N- and C-termini of two different ROD molecules, the ROD β -propeller–Zwilch complex, and the ROD β -propeller complex with the C-terminus of Spindly. The overlapping subcomplexes were superimposed, rigid-body-fitted to the RZZ electron density map, and then manually optimized. Flexible dynamic molecular dynamics fitting (Kidmose *et al*, 2019) and PHENIX real space refinement (Afonine *et al*, 2013) were employed to refine the fit and optimize the model geometries. In almost all regions, the AF2 predictions explained the electron density map very well after minor alterations, but the choice of the lengths of the interacting fragments of ROD was important, as, e.g., the termini of full-length ROD are predicted to interact with themselves since the second ROD molecule is missing, and a prediction of the dimeric full-length complex was not successful.

Data availability

Density maps of RZZ have been deposited into the EMDB with accession code EMD-14120 (<http://www.ebi.ac.uk/pdbe/entry/EMD-14120>). Coordinates of the RZZ complex have been deposited in the PDB with accession code 7QPG (<http://www.rcsb.org/pdb/explore/explore.do?structureId=7QPG>). Original fluorescence and electron microscopy images are available from this link: <https://www.ebi.ac.uk/biostudies/studies/S-BIAD364>

Expanded View for this article is available online.

Acknowledgements

We are grateful to Oliver Hofnagel and Daniel Prumbaum for help in EM data collection, and to the Musacchio and Raunser laboratories for helpful discussion. This work was supported by the Max Planck Society (to A.M. and S.R.). A.M. acknowledges funding by the Marie-Curie Training Network DivIDE (project number 675737), European Research Council (ERC) through Synergy Grant 951430 (BIOMECHANET), and the Deutsche Forschungsgemeinschaft (DFG, German Research Foundation) through SFB1430 (Project-ID 424228829). The authors declare no competing financial interests. Open Access funding enabled and organized by Projekt DEAL.

Author contributions

Tobias Raisch: Formal analysis; Investigation; Visualization; Writing—review & editing. **Giuseppe Ciossani:** Investigation; Visualization; Writing—review & editing. **Ennio d’Amico:** Investigation; Visualization; Writing—review & editing. **Verena Cmentowski:** Investigation; Visualization; Writing—review & editing. **Sara Carmignani:** Resources. **Stefano Maffini:** Resources; Supervision; Writing—review & editing. **Felipe Merino:** Formal analysis; Writing—review & editing. **Sabine Wohlgenuth:** Resources. **Ingrid R Vetter:** Formal analysis; Supervision; Validation; Visualization; Writing—review & editing. **Stefan Raunser:** Funding acquisition; Validation; Project administration; Writing—review & editing. **Andrea Musacchio:** Conceptualization; Supervision; Funding acquisition; Validation; Writing—original draft; Project administration; Writing—review & editing.

In addition to the CRediT author contributions listed above, the contributions in detail are:

AM conceptualized the study. TR, IRV, and FM performed formal analysis. AM and SR acquired funding. VC, GC, Ed’A, and TR investigated the study. AM and

SR contributed to project administration. SC, SM, and SW provided resources. SM, AM, SR, and IRV supervised the study. AM, SR, and IRV validated the study. VC, GC, Ed'A, AM, TR, and IRV visualized the study. AM wrote the original draft. SC, GC, VC, Ed'A, SM, FM, AM, TR, SR, and IRV wrote, reviewed, and edited the manuscript.

Disclosure and competing interests statement

The authors declare that they have no conflict of interest.

References

- Afonine PV, Grosse-Kunstleve RW, Adams PD, Urzhumtsev A (2013) Bulk-solvent and overall scaling revisited: faster calculations, improved results. *Acta Crystallogr D Biol Crystallogr* 69: 625–634
- Alex A, Piano V, Polley S, Stuiver M, Voss S, Ciossani G, Overlack K, Voss B, Wohlgemuth S, Petrovic A et al (2019) Electroporated recombinant proteins as tools for in vivo functional complementation, imaging and chemical biology. *Elife* 8: e48287
- Alieri C, Zhang S, Barford D (2017) Visualizing the complex functions and mechanisms of the anaphase promoting complex/cyclosome (APC/C). *Open Biol* 7: 170204
- Allan LA, Camacho Reis M, Ciossani G, Huis In't Veld PJ, Wohlgemuth S, Kops GJ, Musacchio A, Saurin AT (2020) Cyclin B1 scaffolds MAD1 at the kinetochore corona to activate the mitotic checkpoint. *EMBO J* 39: e103180
- Altenfeld A, Wohlgemuth S, Wehenkel A, Vetter IR, Musacchio A (2015) Complex assembly, crystallization and preliminary X-ray crystallographic analysis of the human Rod-Zwilch-ZW10 (RZZ) complex. *Acta Crystallogr F Struct Biol Commun* 71: 438–442
- Arakel EC, Schwappach B (2018) Formation of COPI-coated vesicles at a glance. *J Cell Sci* 131: jcs218347
- Auckland P, Roscioli E, Coker HLE, McAinsh AD (2020) CENP-F stabilizes kinetochore-microtubule attachments and limits dynein stripping of corona cargoes. *J Cell Biol* 219: e201905018
- Barbosa J, Martins T, Bange T, Tao L, Conde C, Sunkel C (2020) Polo regulates Spindly to prevent premature stabilization of kinetochore-microtubule attachments. *EMBO J* 39: e100789
- Barisic M, Sohm B, Mikolcevic P, Wandke C, Rauch V, Ringer T, Hess M, Bonn G, Geley S (2010) Spindly/CCDC99 is required for efficient chromosome congression and mitotic checkpoint regulation. *Mol Biol Cell* 21: 1968–1981
- Basto R, Gomes R, Kress RE (2000) Rough deal and Zw10 are required for the metaphase checkpoint in *Drosophila*. *Nat Cell Biol* 2: 939–943
- Basto R, Scaerou F, Mische S, Wojcik E, Lefebvre C, Gomes R, Hays T, Kress R (2004) In vivo dynamics of the rough deal checkpoint protein during *Drosophila* mitosis. *Curr Biol* 14: 56–61
- Brohawn SG, Leksa NC, Spear ED, Rajashankar KR, Schwartz TU (2008) Structural evidence for common ancestry of the nuclear pore complex and vesicle coats. *Science* 322: 1369–1373
- Buffin E, Lefebvre C, Huang J, Gagou ME, Kress RE (2005) Recruitment of Mad2 to the kinetochore requires the Rod/Zw10 complex. *Curr Biol* 15: 856–861
- Caldas GV, Lynch TR, Anderson R, Afreen S, Varma D, DeLuca JG (2015) The RZZ complex requires the N-terminus of KNL1 to mediate optimal Mad1 kinetochore localization in human cells. *Open Biol* 5: 150160
- Chan YW, Fava LL, Uldschmid A, Schmitz MH, Gerlich DW, Nigg EA, Santamaria A (2009) Mitotic control of kinetochore-associated dynein and spindle orientation by human Spindly. *J Cell Biol* 185: 859–874
- Cheerambathur DK, Gassmann R, Cook B, Oegema K, Desai A (2013) Crosstalk between microtubule attachment complexes ensures accurate chromosome segregation. *Science* 342: 1239–1242
- Cianfrocco MA, DeSantis ME, Leschziner AE, Reck-Peterson SL (2015) Mechanism and regulation of cytoplasmic dynein. *Annu Rev Cell Dev Biol* 31: 83–108
- Ciossani G, Overlack K, Petrovic A, Huis in 't Veld PJ, Koerner C, Wohlgemuth S, Maffini S, Musacchio A (2018) The kinetochore proteins CENP-E and CENP-F directly and specifically interact with distinct BUB mitotic checkpoint Ser/Thr kinases. *J Biol Chem* 293: 10084–10101
- Civril F, Wehenkel A, Giorgi FM, Santaguida S, Di Fonzo A, Grigorean G, Ciccarelli FD, Musacchio A (2010) Structural analysis of the RZZ complex reveals common ancestry with multisubunit vesicle tethering machinery. *Structure* 18: 616–626
- Cooke CA, Schaar B, Yen TJ, Earnshaw WC (1997) Localization of CENP-E in the fibrous corona and outer plate of mammalian kinetochores from prometaphase through anaphase. *Chromosoma* 106: 446–455
- d'Amico E, Ahmad MUD, Cmentowski V, Girbig M, Müller F, Wohlgemuth S, Brockmeyer A, Maffini S, Janning P, Vetter IR et al (2022) Conformational transitions of the mitotic adaptor Spindly underlie its interaction with Dynein and Dynactin. *bioRxiv* <https://doi.org/10.1101/2022.02.02.478874> [PREPRINT]
- De Antoni A, Pearson CG, Cimini D, Canman JC, Sala V, Nezi L, Mapelli M, Sironi L, Faretta M, Salmon ED et al (2005) The Mad1/Mad2 complex as a template for Mad2 activation in the spindle assembly checkpoint. *Curr Biol* 15: 214–225
- Emsley P, Lohkamp B, Scott WG, Cowtan K (2010) Features and development of Coot. *Acta Crystallogr D Biol Crystallogr* 66: 486–501
- Evans R, O'Neill M, Pritzel A, Antropova N, Senior A, Green T, Židek A, Bates R, Blackwell S, Yim J et al (2021) Protein complex prediction with AlphaFold-Multimer. *bioRxiv* <https://doi.org/10.1101/2021.10.04.463034> [PREPRINT]
- Faesen AC, Thanasoula M, Maffini S, Breit C, Muller F, van Gerwen S, Bange T, Musacchio A (2017) Basis of catalytic assembly of the mitotic checkpoint complex. *Nature* 542: 498–502
- Fath S, Mancias JD, Bi X, Goldberg J (2007) Structure and organization of coat proteins in the COPII cage. *Cell* 129: 1325–1336
- Fava LL, Kaulich M, Nigg EA, Santamaria A (2011) Probing the in vivo function of Mad1:C-Mad2 in the spindle assembly checkpoint. *EMBO J* 30: 3322–3336
- Fotin A, Cheng Y, Sliz P, Grigorieff N, Harrison SC, Kirchhausen T, Walz T (2004) Molecular model for a complete clathrin lattice from electron cryomicroscopy. *Nature* 432: 573–579
- Gama JB, Pereira C, Simões PA, Celestino R, Reis RM, Barbosa DJ, Pires HR, Carvalho C, Amorim J, Carvalho AX et al (2017) Molecular mechanism of dynein recruitment to kinetochores by the Rod-Zw10-Zwilch complex and Spindly. *J Cell Biol* 216: 943–960
- Gassmann R, Essex A, Hu J-S, Maddox PS, Motegi F, Sugimoto A, O'Rourke SM, Bowerman B, McLeod I, Yates JR et al (2008) A new mechanism controlling kinetochore-microtubule interactions revealed by comparison of two dynein-targeting components: SPDL-1 and the Rod/Zwilch/Zw10 complex. *Genes Dev* 22: 2385–2399
- Gassmann R, Holland AJ, Varma D, Wan X, Civril F, Cleveland DW, Oegema K, Salmon ED, Desai A (2010) Removal of Spindly from microtubule-attached kinetochores controls spindle checkpoint silencing in human cells. *Genes Dev* 24: 957–971
- Griffis ER, Stuurman N, Vale RD (2007) Spindly, a novel protein essential for silencing the spindle assembly checkpoint, recruits dynein to the kinetochore. *J Cell Biol* 177: 1005–1015

- ter Haar E, Musacchio A, Harrison SC, Kirchhausen T (1998) Atomic structure of clathrin: a beta propeller terminal domain joins an alpha zigzag linker. *Cell* 95: 563–573
- Hauf S, Cole RW, LaTerra S, Zimmer C, Schnapp G, Walter R, Heckel A, van Meel J, Rieder CL, Peters JM (2003) The small molecule Hesperadin reveals a role for Aurora B in correcting kinetochore-microtubule attachment and in maintaining the spindle assembly checkpoint. *J Cell Biol* 161: 281–294
- Henen MA, Myers W, Schmitt LR, Wade KJ, Born A, Nichols PJ, Vogeli B (2021) The disordered Spindly C-terminus interacts with RZZ subunits ROD-1 and ZWL-1 in the kinetochore through the same sites in *C. elegans*. *J Mol Biol* 433: 166812
- Hoffman DB, Pearson CG, Yen TJ, Howell BJ, Salmon ED (2001) Microtubule-dependent changes in assembly of microtubule motor proteins and mitotic spindle checkpoint proteins at PtK1 kinetochores. *Mol Biol Cell* 12: 1995–2009
- Holland AJ, Reis RM, Niessen S, Pereira C, Andres DA, Spielmann HP, Cleveland DW, Desai A, Gassmann R (2015) Preventing farnesylation of the dynein adaptor Spindly contributes to the mitotic defects caused by farnesyltransferase inhibitors. *Mol Biol Cell* 26: 1845–1856
- Hoogenraad CC, Akhmanova A (2016) Bicaudal D family of motor adaptors: linking dynein motility to cargo Binding. *Trends Cell Biol* 26: 327–340
- Howell BJ, McEwen BF, Canman JC, Hoffman DB, Farrar EM, Rieder CL, Salmon ED (2001) Cytoplasmic dynein/dynactin drives kinetochore protein transport to the spindle poles and has a role in mitotic spindle checkpoint inactivation. *J Cell Biol* 155: 1159–1172
- Jackman M, Marcozzi C, Barbiero M, Pardo M, Yu L, Tyson AL, Choudhary JS, Pines J (2020) Cyclin B1-Cdk1 facilitates MAD1 release from the nuclear pore to ensure a robust spindle checkpoint. *J Cell Biol* 219: e201907082
- Jokelainen PT (1967) The ultrastructure and spatial organization of the metaphase kinetochore in mitotic rat cells. *J Ultrastruct Res* 19: 19–44
- Jumper J, Evans R, Pritzel A, Green T, Figurnov M, Ronneberger O, Tunyasuvunakool K, Bates R, Židek A, Potapenko A et al (2021) Highly accurate protein structure prediction with AlphaFold. *Nature* 596: 583–589
- Karess R (2005) Rod-Zw10-Zwilch: a key player in the spindle checkpoint. *Trends Cell Biol* 15: 386–392
- Kidmose RT, Juhl J, Nissen P, Boesen T, Karlsen JL, Pedersen BP (2019) Namdinator - automatic molecular dynamics flexible fitting of structural models into cryo-EM and crystallography experimental maps. *IUCr* 6: 526–531
- Kops G, Gassmann R (2020) Crowning the kinetochore: the fibrous corona in chromosome segregation. *Trends Cell Biol* 30: 653–667
- Kops GJ, Kim Y, Weaver BA, Mao Y, McLeod I, Yates 3rd JR, Tagaya M, Cleveland DW (2005) ZW10 links mitotic checkpoint signaling to the structural kinetochore. *J Cell Biol* 169: 49–60
- Kuhn J, Dumont S (2017) Spindle assembly checkpoint satisfaction occurs via end-on but not lateral attachments under tension. *J Cell Biol* 216: 1533–1542
- Kuhn J, Dumont S (2019) Mammalian kinetochores count attached microtubules in a sensitive and switch-like manner. *J Cell Biol* 218: 3583–3596
- Kuijt TEF, Lambers MLA, Weterings S, Ponsioen B, Bolhaqueiro ACF, Staijen DHM, Kops G (2020) A biosensor for the mitotic kinase MPS1 reveals spatiotemporal activity dynamics and regulation. *Curr Biol* 30: 3862–3870.e6
- Lara-Gonzalez P, Pines J, Desai A (2021) Spindle assembly checkpoint activation and silencing at kinetochores. *Semin Cell Dev Biol* 117: 86–98
- Lee C, Goldberg J (2010) Structure of coatomer cage proteins and the relationship among COPI, COPII, and clathrin vesicle coats. *Cell* 142: 123–132
- Legal T, Hayward D, Gluszek-Kustusz A, Blackburn EA, Spanos C, Rappsilber J, Gruneberg U, Welburn JPI (2020) The C-terminal helix of BubR1 is essential for CENP-E-dependent chromosome alignment. *J Cell Sci* 133: jcs246025
- Liebschner D, Afonine PV, Baker ML, Bunkoczi G, Chen VB, Croll TI, Hintze B, Hung LW, Jain S, McCoy AJ et al (2019) Macromolecular structure determination using X-rays, neutrons and electrons: recent developments in Phenix. *Acta Crystallogr D Struct Biol* 75: 861–877
- Magidson V, Paul R, Yang N, Ault JG, O'Connell CB, Tikhonenko I, McEwen BF, Mogilner A, Khodjakov A (2015) Adaptive changes in the kinetochore architecture facilitate proper spindle assembly. *Nat Cell Biol* 17: 1134–1144
- Matson DR, Stukenberg PT (2014) CENP-I and Aurora B act as a molecular switch that ties RZZ/Mad1 recruitment to kinetochore attachment status. *J Cell Biol* 205: 541–554
- Maurer-Stroh S, Eisenhaber F (2005) Refinement and prediction of protein prenylation motifs. *Genome Biol* 6: R55
- McEwen BF, Arena JT, Frank J, Rieder CL (1993) Structure of the colcemid-treated PtK1 kinetochore outer plate as determined by high voltage electron microscopic tomography. *J Cell Biol* 120: 301–312
- McKenney RJ, Huynh W, Tanenbaum ME, Bhabha G, Vale RD (2014) Activation of cytoplasmic dynein motility by dynactin-cargo adapter complexes. *Science* 345: 337–341
- Miller SA, Johnson ML, Stukenberg PT (2008) Kinetochore attachments require an interaction between unstructured tails on microtubules and Ndc80 (Hec1). *Curr Biol* 18: 1785–1791
- Mirdita M, Schütze K, Moriowaki L, Ovchinnikov S, Steinegger M (2021) ColabFold - Making protein folding accessible to all. *bioRxiv* <https://doi.org/10.1101/2021.08.15.456425> [PREPRINT]
- Mische S, He Y, Ma L, Li M, Serr M, Hays TS (2008) Dynein light intermediate chain: an essential subunit that contributes to spindle checkpoint inactivation. *Mol Biol Cell* 19: 4918–4929
- Moore SL, Schaber MD, Mosser SD, Rands E, O'Hara MB, Garsky VM, Marshall MS, Pompliano DL, Gibbs JB (1991) Sequence dependence of protein isoprenylation. *J Biol Chem* 266: 14603–14610
- Moriya T, Saur M, Stabrin M, Merino F, Voicu H, Huang Z, Penczek PA, Raunser S, Gatsogiannis C (2017) High-resolution single particle analysis from electron cryo-microscopy images using SPHIRE. *J vis Exp* 123: 55448
- Mosalaganti S, Keller J, Altenfeld A, Winzker M, Rombaut P, Saur M, Petrovic A, Wehenkel A, Wohlgenuth S, Müller F et al (2017) Structure of the RZZ complex and molecular basis of its interaction with Spindly. *J Cell Biol* 216: 961–981
- Moudgil DK, Westcott N, Famulski JK, Patel K, Macdonald D, Hang H, Chan GK (2015) A novel role of farnesylation in targeting a mitotic checkpoint protein, human Spindly, to kinetochores. *J Cell Biol* 208: 881–896
- Musacchio A, Desai A (2017) A molecular view of kinetochore assembly and function. *Biology* 6: 5
- Navarro AP, Cheeseman IM (2021) Kinetochore assembly throughout the cell cycle. *Semin Cell Dev Biol* 117: 62–74
- Nijenhuis W, von Castelmuur E, Littler D, De Marco V, Tromer E, Vleugel M, van Osch MH, Snel B, Perrakis A, Kops GJ (2013) A TPR domain-containing N-terminal module of MPS1 is required for its kinetochore localization by Aurora B. *J Cell Biol* 201: 217–231

- Pagliuca C, Draviam VM, Marco E, Sorger PK, De Wulf P (2009) Roles for the conserved spc105p/kre28p complex in kinetochore-microtubule binding and the spindle assembly checkpoint. *PLoS One* 4: e7640
- Pereira C, Reis RM, Gama JB, Celestino R, Cheerambathur DK, Carvalho AX, Gassmann R (2018) Self-assembly of the RZZ complex into filaments drives kinetochore expansion in the absence of microtubule attachment. *Curr Biol* 28: 3408–3421.e8
- Pettersen EF, Goddard TD, Huang CC, Couch GS, Greenblatt DM, Meng EC, Ferrin TE (2004) UCSF Chimera—a visualization system for exploratory research and analysis. *J Comput Chem* 25: 1605–1612
- Punjani A, Rubinstein JL, Fleet DJ, Brubaker MA (2017) cryoSPARC: algorithms for rapid unsupervised cryo-EM structure determination. *Nat Methods* 14: 290–296
- Punjani A, Zhang H, Fleet DJ (2020) Non-uniform refinement: adaptive regularization improves single-particle cryo-EM reconstruction. *Nat Methods* 17: 1214–1221
- Raaijmakers JA, van Heesbeen R, Blomen VA, Janssen LME, van Diemen F, Brummelkamp TR, Medema RH (2018) BUB1 is essential for the viability of human cells in which the spindle assembly checkpoint is compromised. *Cell Rep* 22: 1424–1438
- Raaijmakers JA, Tanenbaum ME, Medema RH (2013) Systematic dissection of dynein regulators in mitosis. *J Cell Biol* 201: 201–215
- Reck-Peterson SL, Redwine WB, Vale RD, Carter AP (2018) The cytoplasmic dynein transport machinery and its many cargoes. *Nat Rev Mol Cell Biol* 19: 382–398
- Reid TS, Terry KL, Casey PJ, Beese LS (2004) Crystallographic analysis of CaaX prenyltransferases complexed with substrates defines rules of protein substrate selectivity. *J Mol Biol* 343: 417–433
- Rieder CL, Alexander SP (1990) Kinetochores are transported poleward along a single astral microtubule during chromosome attachment to the spindle in newt lung cells. *J Cell Biol* 110: 81–95
- Rodriguez-Rodriguez JA, Lewis C, McKinley KL, Sikirzhyski V, Corona J, Maciejowski J, Khodjakov A, Cheeseman IM, Jallepalli PV (2018) Distinct roles of RZZ and Bub1-KNL1 in mitotic checkpoint signaling and kinetochore expansion. *Curr Biol* 28: 3422–3429.e5
- Rohou A, Grigorieff N (2015) CTFIND4: fast and accurate defocus estimation from electron micrographs. *J Struct Biol* 192: 216–221
- Sacristan C, Ahmad MUD, Keller J, Fermie J, Groenewold V, Tromer E, Fish A, Melero R, Carazo JM, Klumperman J et al (2018) Dynamic kinetochore size regulation promotes microtubule capture and chromosome biorientation in mitosis. *Nat Cell Biol* 20: 800–810
- Santaguida S, Tighe A, D'Alise AM, Taylor SS, Musacchio A (2010) Dissecting the role of MPS1 in chromosome biorientation and the spindle checkpoint through the small molecule inhibitor reversine. *J Cell Biol* 190: 73–87
- Scaerou F, Starr DA, Piano F, Papoulas O, Kares RE, Goldberg ML (2001) The ZW10 and Rough Deal checkpoint proteins function together in a large, evolutionarily conserved complex targeted to the kinetochore. *J Cell Sci* 114: 3103–3114
- Schindelin J, Arganda-Carreras I, Frise E, Kaynig V, Longair M, Pietzsch T, Preibisch S, Rueden C, Saalfeld S, Schmid B et al (2012) Fiji: an open-source platform for biological-image analysis. *Nat Methods* 9: 676–682
- Schlager MA, Hoang HT, Urnavicius L, Bullock SL, Carter AP (2014) In vitro reconstitution of a highly processive recombinant human dynein complex. *EMBO J* 33: 1855–1868
- Sigismund S, Lanzetti L, Scita G, Di Fiore PP (2021) Endocytosis in the context-dependent regulation of individual and collective cell properties. *Nat Rev Mol Cell Biol* 22: 625–643
- Silio V, McAnish AD, Millar JB (2015) KNL1-Bubs and RZZ provide two separable pathways for checkpoint activation at human kinetochores. *Dev Cell* 35: 600–613
- Simonetta M, Manzoni R, Mosca R, Mapelli M, Massimiliano L, Vink M, Novak B, Musacchio A, Ciliberto A (2009) The influence of catalysis on mad2 activation dynamics. *PLoS Biol* 7: e10
- Sivaram MV, Wadzinski TL, Redick SD, Manna T, Doxsey SJ (2009) Dynein light intermediate chain 1 is required for progress through the spindle assembly checkpoint. *EMBO J* 28: 902–914
- Stabrin M, Schoenfeld F, Wagner T, Pospich S, Gatsogiannis C, Raunser S (2020) TransPHIRE: automated and feedback-optimized on-the-fly processing for cryo-EM. *Nat Commun* 11: 5716
- Stagg SM, Gurkan C, Fowler DM, LaPointe P, Foss TR, Potter CS, Carragher B, Balch WE (2006) Structure of the Sec13/31 COPII coat cage. *Nature* 439: 234–238
- Stagg SM, LaPointe P, Balch WE (2007) Structural design of cage and coat scaffolds that direct membrane traffic. *Curr Opin Struct Biol* 17: 221–228
- Starr DA, Williams BC, Hays TS, Goldberg ML (1998) ZW10 helps recruit dynactin and dynein to the kinetochore. *J Cell Biol* 142: 763–774
- Sundin LJ, Guimaraes GJ, Deluca JG (2011) The NDC80 complex proteins Nuf2 and Hec1 make distinct contributions to kinetochore-microtubule attachment in mitosis. *Mol Biol Cell* 22: 759–768
- Tripathi A, Ren Y, Jeffrey PD, Hughson FM (2009) Structural characterization of Tip20p and Dsl1p, subunits of the Dsl1p vesicle tethering complex. *Nat Struct Mol Biol* 16: 114–123
- Tunyasuvunakool K, Adler J, Wu Z, Green T, Zielinski M, Židek A, Bridgland A, Cowie A, Meyer C, Laydon A et al (2021) Highly accurate protein structure prediction for the human proteome. *Nature* 596: 590–596
- Varma D, Monzo P, Stehman SA, Vallee RB (2008) Direct role of dynein motor in stable kinetochore-microtubule attachment, orientation, and alignment. *J Cell Biol* 182: 1045–1054
- Varma D, Wan X, Cheerambathur D, Gassmann R, Suzuki A, Lawrimore J, Desai A, Salmon ED (2013) Spindle assembly checkpoint proteins are positioned close to core microtubule attachment sites at kinetochores. *J Cell Biol* 202: 735–746
- Vassilev LT, Tovar C, Chen S, Knezevic D, Zhao X, Sun H, Heimbrook DC, Chen L (2006) Selective small-molecule inhibitor reveals critical mitotic functions of human CDK1. *Proc Natl Acad Sci USA* 103: 10660–10665
- Wagner T, Merino F, Stabrin M, Moriya T, Antoni C, Apfelbaum A, Hagel P, Sitsel O, Raisch T, Prumbaum D et al (2019) SPHIRE-crYOLO is a fast and accurate fully automated particle picker for cryo-EM. *Commun Biol* 2: 218
- Watson ER, Brown NG, Peters JM, Stark H, Schulman BA (2019) Posing the APC/C E3 ubiquitin ligase to orchestrate cell division. *Trends Cell Biol* 29: 117–134
- Weissmann F, Petzold G, VanderLinden R, Huis in 't Veld PJ, Brown NG, Lampert F, Westermann S, Stark H, Schulman BA, Peters J-M (2016) biGBac enables rapid gene assembly for the expression of large multisubunit protein complexes. *Proc Natl Acad Sci USA* 113: E2564–2569
- Wickham TJ, Davis T, Granados RR, Shuler ML, Wood HA (1992) Screening of insect cell lines for the production of recombinant proteins and infectious virus in the baculovirus expression system. *Biotechnol Prog* 8: 391–396
- Williams BC, Gatti M, Goldberg ML (1996) Bipolar spindle attachments affect redistributions of ZW10, a *Drosophila* centromere/kinetochore component required for accurate chromosome segregation. *J Cell Biol* 134: 1127–1140

- Wojcik E, Basto R, Serr M, Scaerou F, Karess R, Hays T (2001) Kinetochore dynein: its dynamics and role in the transport of the Rough deal checkpoint protein. *Nat Cell Biol* 3: 1001–1007
- Wynne DJ, Funabiki H (2015) Kinetochore function is controlled by a phospho-dependent coexpansion of inner and outer components. *J Cell Biol* 210: 899–916
- Yamamoto TG, Watanabe S, Essex A, Kitagawa R (2008) SPDL-1 functions as a kinetochore receptor for MDF-1 in *Caenorhabditis elegans*. *J Cell Biol* 183: 187–194
- Yang Z, Fang J, Chittuluru J, Asturias FJ, Penczek PA (2012) Iterative stable alignment and clustering of 2D transmission electron microscope images. *Structure* 20: 237–247
- Yao X, Anderson KL, Cleveland DW (1997) The microtubule-dependent motor centromere-associated protein E (CENP-E) is an integral component of kinetochore corona fibers that link centromeres to spindle microtubules. *J Cell Biol* 139: 435–447
- Zhang G, Lischetti T, Hayward DG, Nilsson J (2015) Distinct domains in Bub1 localize RZZ and BubR1 to kinetochores to regulate the checkpoint. *Nat Commun* 6: 7162
- Zheng SQ, Palovcak E, Armache JP, Verba KA, Cheng Y, Agard DA (2017) MotionCor2: anisotropic correction of beam-induced motion for improved cryo-electron microscopy. *Nat Methods* 14: 331–332
- Zivanov J, Nakane T, Scheres SHW (2019) A Bayesian approach to beam-induced motion correction in cryo-EM single-particle analysis. *IUCr* 6: 5–17



License: This is an open access article under the terms of the Creative Commons Attribution-NonCommercial-NoDerivs License, which permits use and distribution in any medium, provided the original work is properly cited, the use is non-commercial and no modifications or adaptations are made.